Title
STRUCTURE AND PROPERTIES OF DYNAMICALLY STRAIN-AGED STEELS.

Author
Page, Elliot W.

Publication Date
1968-06-01

UCRL-18244

Cy. 2

University of California

Ernest O. Lawrence Radiation Laboratory

STRUCTURE AND PROPERTIES OF DYNAMICALLY STRAIN-AGED STEELS

Elliot W. Page

(M.S. Thesis)

June 1968

Berkeley, California

DISCLAIMER

UCRL-18244

UNIVERSITY OF CALIFORNIA
Lawrence Radiation Laboratory
Berkeley, California

AEC Contract No. W-7405-eng-48

STRUCTURE AND PROPERTIES OF DYNAMICALLY STRAIN-AGED STEELS

Elliot W. Page

(M.S. Thesis)

June 1968

TABLE OF CONTENTS

STRUCTURE AND PROPERTIES OF DYNAMICALLY STRAIN AGED STEELS

Elliot W. Page

Inorganic Materials Research Division, Lawrence Radiation Laboratory,
Department of Mineral Technology, College of Engineering,
University of California, Berkeley, California

ABSTRACT

The effect of dynamic strain aging (deformation during aging) upon the mechanical properties and microstructure of Fe-3.5%Cr-0.2%C and Fe-3.5%Mo-0.2%C alloys has been investigated. Dynamic strain aging resulted in a general increase in strength of 10-20% in both alloys with little or no loss in ductility. The mechanical properties were correlated with the observed microstructure using electron microscope techniques. The principle strengthening mechanism in both alloys was found to be due to the increase in dislocation density. Additional strengthening in the Fe-Mo-C alloy was attributed to the deformation enhanced formation of molybdenum carbide.

I. INTRODUCTION

Efforts to improve both the strength and ductility of steel have traditionally centered on modifications in composition or variations in the heat treatment. However, an inverse relationship between strength and ductility is usually observed, with an increase in strength accompanied by a decrease in ductility and visa versa. Increasing the carbon content has been shown to have a dramatic effect on the strength of steel, but appreciable ductility is lost.[1]

The addition of alloying elements which form precipitates can increase strength by retarding dislocation motion, but the lack of dislocation mobility decreases the ductility. Increases in ductility can be obtained by tempering as-quenched materials but strength is lost.

Thermomechanical processes, where plastic deformation is introduced into the heat-treatment cycle, have been developed which increase the strength while obtaining various degrees of ductility. Static strain aging (straining at room temperature before tempering) has resulted in increased strength, but at the expense of a decrease in ductility.[2-4] However, the process of ausforming which consists of plastically deforming metastable austenite prior to transformation to martensite, is capable of producing increases in strength up to 50% with no significant loss in ductility.[5,6]

In ausforming, the strengthening is considered by Thomas et al.[6] to result from an increase in the dislocation density and the pinning of these dislocations by the subsequent formation of alloy carbides. The carbides act not only as a barrier to dislocation motion but also serve as sources for the generation of new dislocations, thus effectively

increasing the dislocation density.

In the past few years the thermomechanical process of dynamic strain-aging has been studied in this laboratory. It is a process where mechanical deformation is applied at elevated temperatures, with aging taking place simultaneously. When applied to ausformed and quenched and tempered steels, dynamic strain-aging increased the strength an additional 10 to 20% without appreciable loss in ductility.[7-9]

Recent work on dynamically strain aged steels[7,10] reveals that although the strength is increased the toughness is maintained.

Although substantial work has been done on the mechanical properties of dynamically strain aged alloys, attempts to examine the microstructure and establish the operative strengthening mechanisms have been inconclusive.[7,8] Zackay et al.[7] suggests that the carbides in dynamic strain-aging act both as dislocation barriers and as sources for dislocation multiplication, similar to the role of the carbides in the ausforming process.[6]

Busch[8] studied the microstructures of dynamically strain aged steels by optical electron microscopy. He observed a strain-induced dispersion of carbides at the temperature of maximum strengthening, but was unable to identify the precipitate. Busch concluded that the probable strengthening mechanism of dynamic strain aging in the carbonless alloys studied involves the strain enhanced diffusion of substitutional solute atoms to dislocations, which in turn, leads to a decrease in dislocation mobility.

Investigations of the response of mild steels (.05% C) to dynamic strain-aging[11] showed that precipitates nucleated on dislocations, and acted as sources for the multiplication of dislocations. A similar

mechanism was attributed to the strengthening which occurs in static strain-aging.[1,4,12] Leslie and Keh[13] suggest that the strengthening in static strain-aging is due to an increase in dislocation density, with precipitation not essential for the strengthening. They do not preclude, however, the possibility of precipitation processes contributing to the strength.

Transmission electron microscopy was utilized in the present study to examine in detail the structure of two dynamically strain-aged martensitic alloys and to determine some of the structural factors involved in the strengthening mechanism. Because of the complex structures obtained in previous work,[7,9] the alloys used in this investigation were of high purity and simple composition. This enables the role of the alloying elements in dynamic strain-aging to be investigated separately in circumstances where the interpretation of structural changes is more readily achieved. Iron-carbon alloys with stoichiometric proportions of molybdenum and carbon and chromium and carbon were used. The alloying elements, molybdenum and chromium, were used since they form alloy carbides at elevated temperatures. The carbon content was fixed at 0.2%C in order to obtain the best combination of strength and ductility.[7,14] Pure iron-carbon steels were to be used as a standard, but due to the low hardenability of the steels of this composition, mixed microstructures were obtained upon quenching and the steels were therefore discarded. As in previous studies,[7-10] all dynamically strain-aged samples were deformed 4 to 6%.

II. EXPERIMENTAL PROCEDURE

A. Preparation

The materials used in this study were vacuum-induction-melted from high purity iron, chromium and molybdenum and cast into 20 lb ingots. The chemical compositions are given in Table I. The as-cast ingots were homogenized for 100 hrs at a temperature of 1100°C in a pure helium atmosphere in order to minimize carburization. Optical microscopy revealed that this treatment was effective.

The ingots were forged and then cut into sections 6" by 3" by 1/8". These sections were austenitized at a temperature of 1200°C for 30 minutes in a pure helium atmosphere, quenched in water, and stored at liquid nitrogen temperatures.

B. Thermomechanical Treatment

The thermomechanical treatments are listed in Table II. To reach the required processing temperatures as quickly as possible, high temperature silicon oil and molten lead baths were used. The oil bath was used for samples processed up to 375°C, and in molten lead for those processed at 500°C. The rolls of the rolling mill were heated to a temperature of approximately 200°C before processing to minimize the heat loss during rolling. Upon reaching processing temperature, the samples were either 1) tempered for 30 minutes and then water-quenched, 2) deformed approximately 5%, then tempered for 30 minutes at processing temperature before water quenching, or 3) tempered 30 minutes before rolling approximately 5% at the processing temperature and then water quenched.

A schematic representation of the thermomechanical treatments are shown in Fig. 1.

C. Mechanical Tests

Tensile specimens 6" by 7/8" by 1/8" with a 2-inch gauge length were machined from each sample. All mechanical testing was done on an Instron machine utilizing a cross-head speed of 0.1 cm/min.

D. Microscopy

Thin foils for electron microscopic observation were prepared from the undeformed grip section of the tensile specimens. Mechanical grinding was used to reduce the grip sections to 0.030 inches. Chemical polishing in H_2O_2 10% HF further reduced them to about 0.003 inches. The samples were electropolished using a modified window technique[15] in an electrolyte of chromic-acetic acids (165 ml acetic acid, 60 gms CrO_3 15 ml H_2O) operated at 12 volts and a temperature of 5°C. During the chemical thinning process a new technique was developed which consists of preferentially thinning the center area of the sample. On subsequent electropolishing small holes appear first near the center of the sample. Foils were cut from the thinned areas around these holes, placed in a double-tilt holder, and examined in a Siemens Elmiskop I electron microscope operated at 100 kV. The usual bright field and gun-tilt dark field techniques of electron microscopy were employed.

Extraction replicas for microscopic examination were prepared by vacuum evaporating a thin layer of carbon on an electro-polished and electrolytically etched surface. The replicas were extracted at a potential of 6 volts in an electrolyte of 10% perchloric acid in acetic

acid. A thin layer of gold was vacuum evaporated on portions of the replica for standardizing the diffraction measurements.

E. Microprobe

Extraction replicas for analysis in an MAC model 400 electron microprobe analyzer were prepared by, 1) mechanically polishing on a special μ diamond polishing wheel, 2) etching for 5 sec in a 2% nital solution, 3) vacuum evaporating a thin layer of carbon on the etched surface, and 4) extracting in a 1% bromine-methanol solution at a temperature of -20°C.

III. RESULTS

A. Mechanical Properties

The tensile properties of the processed steels are tabulated in Tables IV and V. True stress-true strain curves of the Fe-Cr-C steel are plotted in Figs. 2a, b, c for processing temperatures of 25°C (room temperature), 250°C and 375°C, respectively. The upper curves in Figs. 2a,b,c indicate the flow stress before necking of the dynamically strain aged sample, while the lower curve indicates the flow stress of the undeformed tempered martensite. A general increase in flow stress of 10 to 20% is observed upon dynamic strain aging.

The effect of dynamic strain aging upon the tensile properties is shown in Figs. 3, 4, and 5. A plot of .2% offset yield strength as a function of processing temperature is shown in Fig. 3. The dashed curves in both Figs. 3a and 3b indicate the yield strength of the undeformed martensite at various tempering temperatures, while the solid curves show the yield strength after dynamic strain aging at various temperatures. A general increase in yield strength of about 15% was obtained as the result of dynamic strain aging the Fe-Cr-C samples (Fig. 3a). At temperatures above 375°C the alloy begins to soften and the effectiveness of dynamic strain aging decreases.

A general increase of about 20% was obtained upon dynamic strain aging the Fe-Mo-C alloy in the lower temperature range (Fig. 3b). Upon dynamic strain aging at 375°C the Fe-Mo-C alloy showed a secondary hardening peak with a maximum increase in yield strength of 46%. At higher temperatures the alloy becomes overaged resulting in a decreasing effectiveness of dynamic strain aging.

The ultimate tensile strength of the dynamically strain aged steels is similar to those of the yield strength. This is undoubtedly due to the limited amount of work hardening in the dynamically strain aged samples, as shown in Fig. 4. The dashed curves in both Figs. 4a and 4b indicate the tensile strength of the undeformed martensite at various tempering temperatures, while the solid curves show the tensile strength after dynamic strain aging at various temperatures. The increase in tensile strength as a result of dynamic strain aging is only about 5-10% for the Fe-Cr-C alloy (Fig. 4a), but this increase is maintained up to about 400°C.

The Fe-Mo-C alloy shows an increase in tensile strength of 8-10% at the lower processing temperatures, but at 375°C, as a result of secondary hardening, the tensile strength increases 45% upon dynamic strain aging. Above 375°C the effective strengthening due to dynamic strain aging decreases.

The amount of prestrain (nominally 5%) varied slightly throughout the experiment. However, as can be seen from Tables IV and V and Figs. 3 and 4, the fluctuation in the amount of prestrain had no noticeable effect on the resulting strength, with the possible exception of sample 3C, which was inadvertently deformed about 7%. Chung[10] found a linear relationship between the amount of prestraining and the effective strengthening for small amounts of strain, but Wilson and Russell,[16] in agreement with the present results, found that the change in yield strength is very small in the range of 2-7% prior deformation.

A comparison of the magnitude of the strength of the Fe-Cr-C and Fe-Mo-C alloys in Figs. 3 and 4 shows that chromium is a more effective strengthener than molybdenum in both the dynamically strain aged and quenched and tempered samples. Bain[17] found that for an alloying content of more than 3% chromium is the more effective strengthener as shown in Fig. 6.

The effect of dynamic strain aging on the ductility of the Fe-Cr-C and Fe-Mo-C alloys as a function of processing temperature is shown in Fig. 5. The ductility was determined from measurements of the elongation of a 2" gage section during tensile testing. The solid curves in both Figs. 5a and 5b show the elongation upon dynamic strain aging while the dashed curves show the elongation in the undeformed tempered samples.

In general, dynamic strain aging caused a slight decrease in the ductility of the Fe-Cr-C samples as shown in Fig. 5a. At lower temperatures there was a decrease of about 2% in the elongation, while above 375°C the decrease in elongation was about 1%. There is no apparent loss in ductility at 250°C, but this may be due to experimental scatter. In the Fe-Mo-C sample (5b) there was a decrease in elongation of about 2-4% at processing temperatures below 250°C. However, at the processing temperature of 375°C, where the maximum strength was obtained, there was no appreciable loss in ductility upon dynamic strain aging. For processing temperatures above 375°C there was also no significant decrease in ductility.

A comparison of Figs. 3 and 4 with Figs. 5a and 5b reveals that not only do the dynamically strain aged Fe-Cr-C steels have greater strength than the Fe-Mo-C steels, they also have greater residual ductility.

B. Microprobe

The results obtained from microprobe analysis of extraction replicas are summarized in Table VI. Standards of pure Fe, Cr and Mo were used to measure the sensitivity of the radiation to the pure samples. Background counts of Fe, Cr, and Mo were measured on pure C and Cu standards, since the replicas were made with carbon and placed on Cu grids. Since the precipitates are very small relative to the diameter of the beam, the amount of the alloying elements in the precipitate is averaged over the beam area. A polished sample of each steel was used to give an indication of the base level expected. As can be seen from the data in Table VI two samples had counts above the base level. The extraction replica of sample 11C*, which had about 3,500 counts Cr and 5,100 counts Fe, shows some definite evidence of the presence of Cr in the precipitate extracted from this high temperature sample. The extraction replica of sample 11B also had counts above the base level, with about 600 counts Mo and 2,100 counts Fe. This indicates the presence of molybdenum in the precipitate extracted from the sample processed at 500°C.

C. Electron Microscopy

1. Fe-Cr-C Steel.

The effect of dynamic strain aging upon the microstructure of the Fe-Cr-C alloy is revealed in Figs. 7 through 23. The martensitic structure of the as quenched material (sample 1C) is shown in Fig. 7. Widmanstatten-type precipitates are shown in Figs. 7a,b. From the diffraction pattern of Fig. 7c the foil is determined to be oriented with the ⟨111⟩ type direction parallel to the axis of the electron beam,

(e.g., in a ⟨111⟩ type orientation). The long dimension of the precipitates are seen to lie along the three ⟨211⟩ type directions. A trace analysis indicates that the precipitates lie in the {110} habit plane along ⟨111⟩ type directions. The image of the aperture shown at "A" in Fig. 7c indicates the diffraction spots which contribute to the dark field image of the as quenched structure in Fig. 7b. The precipitates in only two of the three ⟨211⟩ type directions shown in Fig. 7a reverse contrast in Fig. 7b. Streaking of the precipitate spots at "B" in Fig. 7c in a direction normal to the $[1\bar{2}1]$ direction indicates that the precipitates are lath-like in shape with the thin direction of the laths in the direction of streaking. The possible existence of twins is observed at "C" in Fig. 7a.

When the as-quenched structure is dynamically strain aged at room temperature (sample 2C, same as static strain aging) the structure appears as shown in Fig. 8. The large block-like areas at "A" in Fig. 8a are oriented along the $[0\bar{1}1]$ direction and reverse contrast in the dark field image in Fig. 8b, as do the precipitates. These block-like areas will be discussed later. The amount of deformation (3.5%) was insufficient to change the basic structure of the martensite needles, but the precipitates within the needles appear to be slightly bent and misoriented. The precipitates in Fig. 8a lie along the $[1\bar{1}0]$ direction when the foil is in a [111] orientation. This is inconsistent with the {110} habit plane previously obtained. This anomaly will be discussed later.

Due to the amount of auto-tempering, little carbon is available for formation or growth of precipitates. Tempering at 125°C (sample 4C) reveals no observable change in the size or number of precipitates.

Dynamic strain aging at 125°C (sample 3C) results in considerable distortion of the shape of the precipitates as shown in Fig. 9. The effect of inadvertently increasing the amount of deformation to 7% instead of 5% is shown by an increase in the distortion of the precipitates (compared with Fig. 8). Although greatly distorted, the precipitates are still discernable in a Widmanstatten pattern with the long axis of the precipitate in a $[33\bar{2}]$ direction when viewed in a [113] orientation (Fig. 9). The precipitates are seen to reverse contrast in the dark field image in Fig. 9b. The observation of dislocation tangles around the precipitates in Fig. 9a suggests that the tempering temperature of 125°C is still sufficiently low to inhibit the motion of dislocations and prevent the relieving of stress concentrations around the precipitates.

Upon tempering at 375°C (sample 10C) the precipitates begin to grow, with a slight increase in both length and width, shown at "A" in Fig. 10. Figure 11 is an enlargement of Fig. 10b with "A" marking the same area in both figures. The precipitates in Fig. 10 can be seen to lie along two [110] type directions with the foil viewed in a [100] orientation.

Dynamic strain aging at 375°C results in the structure shown in Figs. 12, 13, 14, and 15. In Fig. 12 (sample 8C) the precipitates are in a Widmanstatten pattern with the axis of the precipitates along the $\langle 11\bar{2} \rangle$ type directions in a $[11\bar{1}]$ orientation. Figures 12a and 12b are the same identical area, differing only slightly in orientation. Figure 13 is an enlargement of Fig. 12a. The letter "A" marks areas which coincide in Figs. 12, 12b, and 13. A fine dispersion of precipitates which nucleate on dislocations is observed at "B" in Fig. 13. Figure 14 (sample 9C) is in a [111] orientation with the precipitates along

the three ⟨211⟩ directions as shown in Fig. 14c. Figure 14b is an enlargement of Fig. 14a with "A" marking corresponding areas. Some precipitates, marked at "B" in Fig. 14b, are bent and distorted in shape. New small round precipitates are observed near "C" in Fig. 14b. Figure 15 is another example of the structure of sample 9C. It is also in a [111] orientation with the precipitates in a Widmanstatten pattern along the ⟨211⟩ type directions. The precipitates reverse contrast in the dark field image shown at "A" in Fig. 15b.

Tempering at 500°C (sample 13C) results in the partial spheroidization of the precipitates which lie along the [2$\bar{3}\bar{3}$] direction in a [311] orientation as shown in Fig. 16. Also present is a more randomly oriented precipitate. Evidence of the recovery of dislocations and relieving of grain boundary stresses can be observed at "A" in Fig. 16.

Deforming, then tempering, at 500°C (sample 11C) results in a noticeable decrease in the precipitation density due to the spheroidization and dissolution of the precipitate as shown in Fig. 17. The precipitates are still visible in a Widmanstatten pattern with the long axis of the precipitate along the three ⟨211⟩ type directions when viewed in a [111] orientation. Also visible in Fig. 17 are very small, randomly oriented precipitates seen more clearly in the dark field image of Fig. 17b, to the right of "A". Figure 18 (also sample 11C) shows the initial stages of recrystallization at "A", precipitation on dislocations at "B" and dissolution of the precipitate at "C".

Tempering at 600°C (sample 13C*) results in a considerable amount of recrystallization, and rapid spheroidization of the precipitates as shown in Fig. 19. Due to this spheroidization no definite orientation

of the precipitates is discernable. Also present in Fig. 19 is a very fine dispersion of precipitate spots shown near "A" in Fig. 19b. An extraction replica of sample 13C* shown in Fig. 20 reveals the spheroidized structure. The streaking of precipitate spots in Fig. 20b indicates the thin direction of the precipitates.

Tempering sample 11C at 600°C (sample 11C*) reveals extensive recovery and recrystallization with polygonization visible at "A" in Fig. 21. Small precipitate dots are observed near "B" in Fig. 21a with the precipitate contrast reversed in the dark field image of Fig. 21b. The aperture at "C" in Fig. 21c marks the precipitate spot responsible for the dark field image. The foil is in a [111] orientation with the $[2\bar{1}\bar{1}]$ direction indicated in Fig. 21c.

Another example of the recovered structure of sample 11C* is shown in Fig. 22 (bright field image) and Fig. 23 (dark field image). In Figs. 22 and 23, "A" shows dislocations lining up during recovery. Fine precipitates can be seen to the left of "B", and extensive polygonization exists at "C".

2. Fe-Mo-C steel.

The effect of dynamic strain aging upon the microstructure of the Fe-Mo-C alloy is revealed in Figs. 24-32. The as quenched structure of sample 1B appears quite similar to the structure of sample 1C. The precipitates are observed in Fig. 24 to lie along the three ⟨211⟩ type direction when viewed in a ⟨111⟩ orientation. Evidence of twinning can be seen at "A" in Fig. 24.

Dynamic strain aging the as quenched material (sample 2B) caused a slight distortion of the precipitates (not shown).

Tempering at 125°C (sample 4B) and 250°C (sample 7B) caused little change in the size of the precipitates and only a slight increase in the number of precipitates. Dynamic strain aging at 125°C (sample 3B) and 250°C (samples 5B to 6B) caused a distortion of the precipitates.

Tempering at 375°C (sample 10B) resulted in a slight broadening and possible initial dissolution of the precipitates, but little or no increase in length was observed as shown in Fig. 25. When viewed in a [311] orientation, the precipitates lie along the $[2\bar{3}\bar{3}]$ direction and two $\langle 10,1,3 \rangle$ type directions as shown in Fig. 25. The contrast is reversed in the dark field image of Fig. 25b. Dislocations are visible to the left of "A" in Fig. 25a with a noticeable lack of precipitation on the dislocations.

Deforming before tempering at 375°C (sample 8B) results in the initial stages of dissolution of the precipitate as shown in Fig. 26a. The precipitates have grown slightly in both length and width in comparison with sample 1B, Fig. 24, but are still in a Widmanstatten pattern along the $\langle 211 \rangle$type directions in a [111] orientation. Streaking of the precipitate spots at B in Fig. 26c perpendicular to the $\langle 211 \rangle$ directions indicates that the precipitates are lath-shaped and lie along the $\langle 211 \rangle$ directions. Figure 26b is an enlargement of Fig. 26a. Small new precipitates are visible near "A" in Fig. 26b.

Another example of these small new precipitates are seen in Fig. 27a. Using the matrix and precipitate spot marked in Fig. 27c these new precipitates and the dislocation are seen to reverse contrast at "A" in

Fig. 27b. The foil is in a ⟨100⟩ orientation with the large precipitates along ⟨110⟩ directions.

Tempering at 500°C (sample 13B) results in the rapid growth of the precipitates. Some of the precipitates become quite large as seen in Fig. 28. The precipitates are seen to lie along the [1$\bar{1}$1] direction when viewed in a [110] orientation. Analysis of the diffraction pattern will be discussed later. Tempering, then deforming at 500°C (sample 12B) results in the structure shown in Fig. 30. Both large and small precipitates are seen to lie along the ⟨211⟩ type directions when reviewed in a [111] orientation. The precipitates reverse contrast in the dark field image of Fig. 30b. An extraction replica of sample 12B reveals large precipitates which appear to be growing along martensitic grain boundaries.

Tempering at 600°C (sample 13B*) results in the almost complete dissolution of the precipitates (shown at "B" in Figs. 31a,b). The area of the diffraction pattern contributing to the dark field image is shown at "A" in Fig. 31c. Streaking of the matrix spot perpendicular to the ⟨100⟩ type direction in Fig. 31c indicates the possible initial formation of a new precipitate along the ⟨100⟩ direction. The precipitate like lines in Fig. 31b are seen to reverse contrast in the dark field image of Fig. 31a.

Additional tempering of sample 12B at 600°C (sample 12B*) reveals the spheroidizing and dissolving of the precipitate, shown at "A" in Fig. 32. Also present in Fig. 32 is precipitation along the projection of the ⟨100⟩ direction in the ⟨113⟩ orientation. Both new and dissolving precipitates are seen to reverse contrast in the dark field image formed

by the precipitate spots shown at B in Fig. 32c. Streaking of the precipitate spots indicates the thin direction of the precipitate. One of the streaked spots lies perpendicular to the ⟨100⟩ direction.

IV. DISCUSSION

The results obtained in both the Fe-Cr-C and Fe-Mo-C steels are similar in many respects. The formation and structure of the martensite, which is equally applicable to both steels, will be included in the discussion of the Fe-Cr-C steel. Comparisons between the structure and properties of the two steels will be included in the discussion of the Fe-Mo-C steel.

A. Fe-Cr-C Steel

Due to the low carbon content and low alloy content of the steels used in this investigation, the martensitic transformation temperature is rather high ($M_s \approx 445$ for Fe-Cr-C alloy).[36] This high M_s temperature enables the martensite formed upon transformation to temper during the remainder of the quench, forming auto-tempered precipitates in a Widmanstatten pattern. This type of structure is commonly observed.[19-23] Baker et al.[19] observed auto-tempered plates or lathes 100 Å by 1500 Å long in a Widmanstatten pattern. Kurdjumov[20] found that in carbon steels containing less than 0.6% carbon, partial auto-tempering of martensite occurs even with the most drastic quenching. This auto-tempered structure was observed in all samples of both alloys (Figs. 7-32). Analysis of the diffraction patterns identified the precipitate to be cementite in all samples (Fe_3C). The structure of the cementite was obtained from the large single cementite grain shown in Fig. 28a. The diffraction spots of the cementite lattice were consistently indexed in Fig. 28b. It was determined that the cementite precipitates on the $(110)_\alpha$ plane of the matrix along the $\langle 111 \rangle_\alpha$ type directions. This agrees with previous

investigators,[19,21,24-27] and is consistent with the trace analysis of all figures (Figs. 7-32) in this investigation, except Fig. 8.

In the as-quenched structure the martensite can appear in the form of plates as well as needles or laths. Kelly and Nutting[21,22] found that in 0.2% C steels, slightly more than 2% of the martensite forms as twin plates. Although a small percentage of martensite formed as twins in this investigation examples of these twins are shown at "C" in Fig. 7 and at "A" in Fig. 24. The large block like areas in Fig. 8 also appear to be twins. These areas are concluded not to be precipitates because of their size, orientation, and lack of precipitate spots in the diffraction pattern (not shown). They are considered not to be martensite needles viewed end on because they appear within other martensitic needles. Such a configuration would be inconsistent with their formation by a shear transformation.[21]

Although no twin spots appeared in the diffraction pattern of Fig. 8, these areas could still be twins since in a [111] orientation, twinning on a $[\bar{2}11]$ twin plane results in twin spots which all coincide with the matrix spots,[41] making the twin spots unobservable. Shimizu,[29] in electron microscopy studies of Fe-Ni martensite, observed band-like structures similar to those in Fig. 8 which he identified as twin ribbons in the $\langle 111 \rangle$ direction on $\{211\}$ twin planes. When viewed in a $\langle 111 \rangle$ orientation these twins would project as a band along the $\langle 110 \rangle$ direction. This is what is observed in Fig. 8 and it is concluded that these block-like areas are large twin plates. The observation of the precipitates along the $\langle 110 \rangle$ type directions in a $\langle 111 \rangle$ orientation in Fig. 8 instead

of the expected ⟨211⟩ type direction can be explained by the extensive twinning observed in the sample in Fig. 8.

The increase in flow stress in Fig. 2 can either be the result of an increase in dislocation density or the formation of clusters or precipitates which act as barriers to dislocation motion. However, careful observation of Figs. 7 and 8 and Figs. 10 and 12 reveals the same precipitate density at 25°C as at 375°C. If clusters or small precipitates were forming at 25°C, these precipitates would become evident upon tempering. Also, the increase in flow stress in Fig. 2 due to dynamic strain aging is independent of the processing temperature. From these observations it is concluded that the formation of clusters or precipitates is not the cause of the increase in flow stress. But since the shear type mechanism in the martensitic transformation[21] causes a very high dislocation density in the undeformed as-quenched condition, the increase in dislocation density resulting from a 5% deformation would be undetectable. Also, observation of dislocations in a foil depends greatly on the contrast condition.[31] As can be seen in Fig. 12, a slight change in the orientation considerably changes the contrast effects making estimates of the dislocation density difficult.

Kelly and Nutting[22] estimate the dislocation density in untempered martensite to be about $1\times10^{12}/cm^2$. After a 5% deformation the dislocation density can be calculated from flow stress relationships[30] to be about $2\times10^{12}/cm^2$. This increase in dislocation density is unresolvable in the electron microscope. However, distortion of the precipitates in Figs. 9 and 14 upon dynamic strain aging indicates the motion and thus the subsequent multiplication of dislocations. From these observations, it is concluded that the increase in flow stress due to dynamic strain aging (Fig. 2) is probably due to an increase in dislocation density.

Two types of dynamic strain aging processes were studied at 375°C. One process consisted of deforming and subsequently tempering the sample at 375°C (sample 8C), while in the other process the sample was tempered before deforming at 375°C (sample 9C). A comparison of samples 8C and 9C with the sample that was only tempered at 375°C (sample 10C) reveals a noticeable difference in precipitate structure. Besides the cementite precipitates in Fig. 11, sample 10C, a fine structure can be seen to the left of "A" in Fig. 11 which reveals dislocations in a dotted contrast,[31] but very little precipitation on the dislocations is evident. In contrast, the samples dynamically strain aged at 375°C show not only the Widmanstatten cementite precipitates, but also a new finely dispersed phase on dislocations (Figs. 12, 13, 14, 15). Careful observation of the dislocations in Figs. 13 and 14 shows that the dislocations are not bowed around the new precipitates. This indicates that precipitation occurred on the dislocations after deformation. Examination of the diffraction pattern shown in Fig. 14c reveals only cementite to be present. This suggests that the new precipitates are also cementite. It seems likely that the dislocations introduced into the sample upon deformation became favorable sites for additional precipitation of cementite from carbon contained in the matrix. Another possible source of carbon could be the partial dissolution and reprecipitation of existing cementite laths. Kurdjumov[20] found that the presence of alloying elements such as Cr and Mo, leads to an increase in the stability of a supersaturated solid solution of low carbon content. But Fopiano[23] indicated that a dissolution and reprecipitation of cementite can occur on aging after deformation.

Deforming, then tempering at 125°C results in the distortion of the precipitates but the temperature appears to be insufficient to allow relaxation of the dislocations and reshaping of the precipitates upon tempering as shown in Fig. 9. Comparison of Fig. 12 (sample 8C) with Fig. 14 (sample 9C) shows that tempering after deforming at 375°C (Fig. 12) allows the dislocations around the auto-tempered precipitates to relax. The tempering also allows the precipitates to reshape into sharp but broadened needles. The diffusion of carbon in the matrix at 375°C is almost instantaneous,[32] permitting the rapid redistribution of carbon. However, tempering before deforming (Fig. 14) results in the growth, then distortion of the cementite precipitates shown at "B" in Figs. 14b and 15.

Dynamic strain aging at 500°C (sample 11C) reveals a structure in which the auto-tempered cementite is beginning to dissolve and spheroidize (Fig. 17). Also observed in Fig. 17b are small randomly oriented precipitates presumably those precipitates which formed on the dislocation from the possible dissolution of cementite after deformation. From Fig. 18 it appears that these newly formed precipitates are more stable than the auto-tempered cementite. This might be explained by the high solubility of chromium in cementite.[33-35] (Kuo[33] found that chromium can replace as much as 20% of the iron in cementite.) Since the diffusion of chromium atoms in deformed martensite at 500°C is appreciable, it is expected that chromium atoms would diffuse into the newly formed precipitates and more readily than into the cementite already formed. The chromium in the cementite would tend to stabilize the precipitates and inhibit their resolution. This stabilization of the cementite would be expected to

contribute somewhat to the strengthening of the alloy. A slight stabilization of the strength level is observed in Figs. 3a and 4a at 375°C. However, the rapid increase in dislocation mobility at 500°C is probably the controlling factor which results in the alloy softening considerably.[35] These new precipitates might also be the initial formation of Cr_7C_3, whose formation has been accelerated by deformation enhanced diffusion.[33-35] But no evidence of Cr_7C_3 was detected in the analysis of the diffraction patterns even at higher temperatures. However the high solubility of chromium in cementite makes the detection of Cr_7C_3 extremely difficult since the d spacing of Cr_7C_3 and Fe_3C are very close. Microprobe analysis of precipitates extracted from sample 11C* indicates the existence of a considerable amount of chromium in the extracted precipitates, suggesting the presence of Cr_7C_3. However, since Cr_7C_3 probably forms in situ from Fe_3C,[33-34] the small secondary precipitation observed on dislocations at 375°C is most likely Fe_3C.

A comparison of Figs. 16, 17, 19, and 21 shows that these new precipitates are not as evident in sample 13C (Fig. 16, which was tempered at 500°C) as they are in sample 11C (Fig. 17, which was dynamically strain aged at 500°C). Tempering at 600°C (sample 13C*) results in the growth of these precipitates (Fig. 21). From these observations it can be seen that dynamic strain aging enhances the tempering process, with the magnitude of enhancement estimated to be about 100°C.

B. Fe-Mo-C Steel

The as-quenched structure of the Fe-Mo-C alloy (sample 1B, Fig. 24) appears quite similar to that of the Fe-Cr-C alloy. Due to the high martensitic transformation temperature ($M_s \approx 405°C$)[36] auto-tempered cementite precipitates formed within the martensite needles on the {110} planes along the ⟨111⟩ directions as discussed previously. The extent of the auto-tempering in the Fe-Mo-C alloy appears to be less than that in the Fe-Cr-C alloy (compare Figs. 7 and 24). This is consistent with the lower M_s temperature of the Fe-Mo-C alloy. As in the Fe-Cr-C alloy twinning occurs only in a small percentage of the martensite laths in the Fe-Mo-C alloy as shown at "A" in Fig. 24.

Dynamic strain aging at temperatures below 375°C results in the distortion of the precipitates due to the interaction of the precipitate with the dislocations introduced upon deformation as explained in the previous section. This increase in dislocation density results in an increase in yield strength of 10-20% in the Fe-Mo-C alloy (Fig. 3b).

Dynamic strain aging at 375°C results in the initial stages of dissolution of the auto-tempered cementite and the formation of new precipitates on dislocations (Figs. 26,27). Comparison of Figs. 26 and 27 with Fig. 25 reveals that there are noticeably fewer of these new precipitates in the undeformed sample (Fig. 25). This demonstrates the effect of dynamic strain aging in accelerating the formation of precipitates. The observation that the dislocations are not bowed

around the precipitates indicates that precipitation occurred on the dislocations after deformation. Analysis of the diffraction patterns in Figs. 26c and 27c reveals only cementite to be present. This suggests that the new precipitates are also cementite. However, the formation of molybdenum rich clusters or Mo_2C precipitates, which are too small to be visible in Figs. 26 and 27 and in the diffraction patterns of Figs. 26c and 27c might be responsible for the secondary hardening peak observed in Figs. 3b and 4b. Homeycombe et al.,[37,38] in work on the secondary hardening in Fe-4% Mo-0.2% C steels, observed streaking of matrix spots in the ⟨100⟩ type directions (the expected direction for Mo_2C) at peak hardness and very small precipitates of Mo_2C just after peak hardness. The elongation of the diffraction spot in the ⟨100⟩ trace direction, and the reversal of contrast for both the precipitates and the dislocation in Fig. 27b indicates that both a matrix spot and a precipitate spot contributed to the dark field image. This suggests the possible existence of Mo_2C upon dynamic strain aging at 375°C. Tempering at 600°C also shows the streaking of the diffraction spots perpendicular to the ⟨100⟩ trace direction (Fig. 31c). The bright field and dark field images of Fig. 31 show a different precipitate morphology than in all previous samples. In Fig. 31 fine precipitate-like areas are seen to be along the trace of the ⟨100⟩ direction. From the streaking of the diffraction spots and from the reversal of contrast in Fig. 31a it appears that these areas are Mo_2C clusters which have precipitated along dislocations which lie in a ⟨100⟩ type direction. Raynor et al.[40] in an extensive investigation of the initial stages of Mo_2C formation,

found that the apparent streaking of the matrix spots, as in Fig. 31c, was actually streaking of Mo_2C precipitate spots that closely coincided with the matrix spots. Dynamic strain aging at 500°C and additional tempering at 600°C results in a fine precipitate structure along the ⟨100⟩ trace direction (Fig. 32). Analysis of the diffraction pattern in Fig. 32c and comparison of the diffraction patterns with a schematic pattern presented by Raynor,[40] identifies the precipitates in sample 12B* to be Mo_2C.

A comparison of Fig. 31 and Fig. 32 reveals that dynamic strain aging accelerates the formation of Mo_2C. In Fig. 31 the precipitates are clustered along the dislocation causing streaking of the diffraction spots, but reveal no Mo_2C pattern, while in the dynamically strain aged sample (Fig. 32) the Mo_2C has formed fine needle-like precipitates with identifiable precipitate spots in the diffraction pattern.

Because of its atomic size, molybdenum diffuses relatively slowly in the matrix even at 600°C even though dynamic strain aging enhances the diffusion of the molybdenum atoms. The slow diffusion of molybdenum results in the slow growth of Mo_2C.[34] This suggests that clusters or very fine Mo_2C precipitates can form in samples dynamically strain aged at 375°C, but they may not be visible until dynamic strain aging for one hour at 600°C.

Since Mo_2C nucleates separately from cementite in a fine dispersion which causes secondary hardening, it follows that the strengthening observed in the Fe-Mo-C alloy which was dynamically strain aged at 375°C (Figs. 3b and 4b) results from the initial formation of Mo_2C.

A corresponding formation of alloy carbides in the Fe-Cr-C alloy is not observed because of the high solubility of chromium in cementite. In contrast molybdenum is only slightly soluable in cementite. This allows the molybdenum to precipitate separately.

V. SUMMARY AND CONCLUSIONS

The effect of dynamical strain aging upon the mechanical properties and microstructure of Fe-3.5%Cr-0.2%C and Fe-3.6%Mo-0.2%C steels has been investigated. Chromium has been found to be a more effective strengthener than molybdenum at these alloy contents, as well as attaining greater ductility. The Fe-Cr-C steel maintained a general increase in strength of 10-15 percent due to dynamic strain aging up to temperatures of about 400°C. The Fe-Mo-C steel showed a general increase in strength of 15-20% due to dynamic strain aging, with an additional 25% increase in strength at 375°C, attributed to the formation of Mo_2C, which is observed only in the over-aged samples.

Small precipitates observed near peak strength in both steels indicates that they are not alloy carbides, but new cementite precipitates which have reprecipitated on dislocation during dynamic strain aging.

The main results may be summarized as follows:

1. The general strengthening mechanism in both steels was attributed to the increase in dislocation density upon dynamic strain aging.
2. Dynamic strain aging results in a general increase in strength of 10-20% in both steels with little or no loss in ductility.
3. Dynamic strain aging tends to decrease the elongation at lower temperatures, but at higher temperatures maintains comparable ductility.
4. A maximum increase in strength of 45% was achieved in the Fe-Mo-C steel, due to the apparent deformation enhanced formation of Mo_2C combined with the probable increase in dislocation density.

ACKNOWLEDGMENTS

The author is deeply grateful to Professor V. F. Zackay, Professor G. Thomas and P. Manganon and J. Hall for their guidance, encouragements and discussion throughout the course of this investigation. He would also like to thank John Blunden, Gloria Pelatowski and Pat Shand for their technical assistance.

This work was performed under the auspices of the United States Atomic Energy Commission.

REFERENCES

1. G. R. Speich and H. Warlimont, J. Iron Steel Inst. 206, 385 (1968).

2. E. B. Kula, in Strengthening Mechanisms, Metals and Ceramics, J. J. Burke, N. L. Reed and V. Weiss, eds. (Syracuse University Press, Syracuse, N.Y., 1966), p. 83.

3. E. T. Stephenson and M. Cohen, Trans ASM 54, 72 (1961).

4. A. S. Keh and W. C. Leslie, Materials Science Research, H. H. Stadelmaier, ed. (John Wiley and Sons, Inc., New York, N. Y., 1963), p. 208.

5. D. J. Schmatz, Met. Eng. Quart. ASM, 6 (2), 20 (1966).

6. G. Thomas, D. Schmatz, and W. W. Gerberich, in High Strength Materials, V. F. Zackay, ed. (John Wiley and Sons, Inc., New York, N.Y., 1965), p. 251.

7. V. F. Zackay, W. Gerberich, R. Busch and E. R. Parker, Lawrence Radiation Laboratory, Berkeley, California, UCRL-16363, October 1965.

8. R. A. Busch, Ph.D. Thesis, University of California, Berkeley, Lawrence Radiation Laboratory, Berkeley, California, UCRL-17805, September 1967.

9. V. S. Goel, Ph.D. Thesis, University of California, Berkeley, Lawrence Radiation Laboratory, Berkeley, California, UCRL-11569, January 1965.

10. Y. Chung, M.S. Thesis, University of California, Berkeley, Lawrence Radiation Laboratory, Berkeley, California, UCRL-18116, March, 1968.

11. B. J. Brindley and J. T. Barney, Acta Met. 14, 1765 (1966).

12. A. S. Keh and H. A. Wriedt, Trans. AIME, 224, 560 (1962).

13. W. C. Leslie and A. S. Keh, J. Iron Steel Inst. 200, 722 (1962).

14. G. R. Chanani, M. S. Thesis, University of California, Berkeley, Lawrence Radiation Laboratory, Berkeley, California, UCRL-17805, September 1967.

15. G. Thomas, in Transmission Electron Microscopy of Metals, (John Wiley and Sons, Inc., New York, N. Y., 1962), p. 150.

16. D. Wilson and B. Russell, Acta Met. 8, 468 (1960).

17. E. Bain and H. W. Paxton, in Alloying Elements in Steels, 2nd. ed. (ASM, Metals Park, Ohio, 1961), p. 148.

18. P. Manganon, unpublished work, University of California, Lawrence Radiation Laboratory, Berkeley, California.

19. A. J. Baker, P. M. Kelly and J. Nutting, in Electron Microscopy and Strength of Crystals, G. Thomas and J. Washburn, eds. (Interscience Publishers, New York, N. Y. 1963), p. 899.

20. G. V. Kurdjumov, J. Iron Steel Inst. 198, 26 (1960).

21. P. M. Kelly and J. Nutting, Proc. Roy. Soc. 259, 45 (1960).

22. P. M. Kelly and J. Nutting, J. Iron Steel Inst. 199, 199 (1961).

23. P. J. Fopiano, S. Das Gupta and D. Kalish, ManLabs, Inc. Tech. Rept. 320.4/4-3, June 1962.

24. K. Tekin, P. M. Kelly, in Precipitation from Iron-Base Alloys, G. R. Speich and J. B. Clark, eds (Gordon and Breach Science Publishers, New York, N. Y., 1965), p. 173.

25. W. C. Leslie, Acta Met. 9, 1004 (1961).

26. W. Pitsch and A. Schrader, Arch. Eisen. 29, 485 (1958).

27. G. R. Srinivasan and C. M. Wayman, 16, 609 (1968).

28. C. M. Wayman, Iron Steel Inst. Special Report 93, 153 (1965).

29. K. Shimizu, J. Phys. Soc. Japan, 17 (3), 508 (1962).

30. A. S. Keh and S. Weissman, in Electron Microscopy and Strength of Crystals, G. Thomas and J. Washburn, eds. (Interscience Publishers, New York, N. Y., 1963), p. 231.

31. P. B. Hirsch, A. Howie, M. J. Whelan, et al., Electron Microscopy of Thin Crystals, (Butterworths, New York, N. Y., 1965), p. 247.

32. G. S. Ansell and A. Arrott, Trans. AIME, 227, 1080 (1963).

33. K. Kuo, J. Iron Steel Inst. 173, 363 (1953).

34. J. H. Woodhead, A. G. Quarrell, J. Iron Steel Inst. 203, 605 (1965).

35. E. Smith, J. Nutting, J. Iron Steel Inst. 185, 314 (1957).

36. K. W. Andres, J. Iron Steel Inst. 203, 721 (1965).

37. R. W. K. Honeycomb, H. J. Harding, J. J. Irani, in High Strength Materials, V. F. Zackay, ed. (John Wiley and Sons, Inc., New York, N. Y., 1965), p. 213.

38. J. J. Irani and R. W. K. Honeycombe, J. Iron Steel Inst. 203, 826 (1965).

39. G. H. Karchner and E. T. Stephenson, Trans. ASM 60, 716 (1967).

40. D. Raynor, J. A. Whiteman and R. W. K. Honeycombe, J. Iron Steel Inst. 204, 349 (1966).

41. O. Johari and G. Thomas, Trans. AIME, 230, 597 (1964).

Table I. Chemical analysis; chemical composition, wt.%.

Sample	% C	% Alloying element	Balance
B =	.187	3.38 Mo	Fe
C =	.186	3.58 Cr	Fe

Table II. Thermomechanical treatment of Fe-Cr-C steel.

Sample	Processing Temp. °C	% Deformed (Rolling)	Treatment
1C	25	0	0
2C	25	4.43	□
3C	125	6.78	□
4C	125	0	0
5C	250	5.74	□
6C	250	5.74	△
7C	250	0	0
8C	375	5.00	□
9C	375	5.00	△
10C	375	0	0
11C	500	3.50	□
12C	500	5.26	△
13C	500	0	0
11C*	600	3.50	□*
13C*	600	0	0*

0 = tempered 30 min. at temp.

□ = deformed then tempered 30 min. at temp.

△ = tempered 30 min. at temp. then deformed.

* = tempered 30 additional min. at 600°C.

+ All samples were water quenched immediately after processing.

Table III. Thermomechanical treatment of Fe-Mo-C steel.

Sample	Processing Temp. °C	% Deformed (Rolling)	Treatment
1B	25	0	0
2B	25	3.51	□
3B	125	5.93	□
4B	125	0	0
5B	250	5.78	□
6B	250	6.32	Δ
7B	250	0	0
8B	375	5.76	□
9B	375	5.17	Δ
10B	375	0	0
11B	500	3.52	□
12B	500	5.34	Δ
13B	500	0	0
12B*	600	5.34	Δ*
13B*	600	0	0*

0 = tempered 30 min. at temp.

□ = deformed then tempered 30 min. at temp.

Δ = tempered 30 min. at temp. then deformed.

* = tempered 30 additional min. at 600°C.

+ All samples were water quenched immediately after processing.

Table IV. Tensile Properties of Fe-Cr-C steel.

Sample	Yield 0.2% (ksi)	Ultimate (ksi)	Elongation (%)	Treatment
1C	168	191	6.80	O
2C	191	199	5.88	□
3C	200	208	4.94	□
4C	162	186	7.58	O
5C	184	193	6.75	□
6C	181	194	6.06	Δ
7C	162	185	6.88	O
8C	187	194	5.44	□
9C	181	189	4.60	Δ
10C	159	180	6.85	O
11C	142	152	6.95	□
12C	146	156	5.71	Δ
13C	142	154	8.56	O

O = tempered 30 min. at temp.

□ = deformed then tempered 30 min. at temp.

Δ = tempered 30 min. at temp. then deformed.

Table V. Tensile Properties of Fe-Mo-C steel.

Sample	Yield 0.2% (ksi)	Ultimate (ksi)	Elongation (%)	Treatment
1B	137	165	6.08	0
2B	174	179	4.36	□
3B	170	174	3.88	□
4B	142	159	6.41	0
5B	164	169	*	□
6B	165	171	3.82	Δ
7B	138	161	6.77	0
8B	179	182	4.11	□
9B	183	196	3.96	Δ
10B	124	135	4.37	0
11B	145	153	8.48	□
12B	165	172	5.05	Δ
13B	125	139	8.99	0

0 = tempered 30 min. at temp.

□ = deformed then tempered 30 min. at temp.

Δ = tempered 30 min. at temp. then deformed.

* = broke outside gage section.

Table VI. Microprobe results.

Specimen	Counts/10 sec		
	Fe	Cr	Mo
Fe (stand.)	24,813	24	8
Cr (stand.)	30	18,370	5
Mo (stand.)	65	42	6,910
C (stand.)	10	10	5
Cu (stand.)	35	30	5
11C*(sample)	24,600	900	--
8B (sample)	22,600	---	190
11C* (replica)	5,230	3,520	--
10C	2,250	140	--
8C	4,450	200	--
1C	70	30	--
12B	550	---	145
11B	2,130	---	610
10B	3,870	10	100
8B	280	---	25
1B	405	---	160

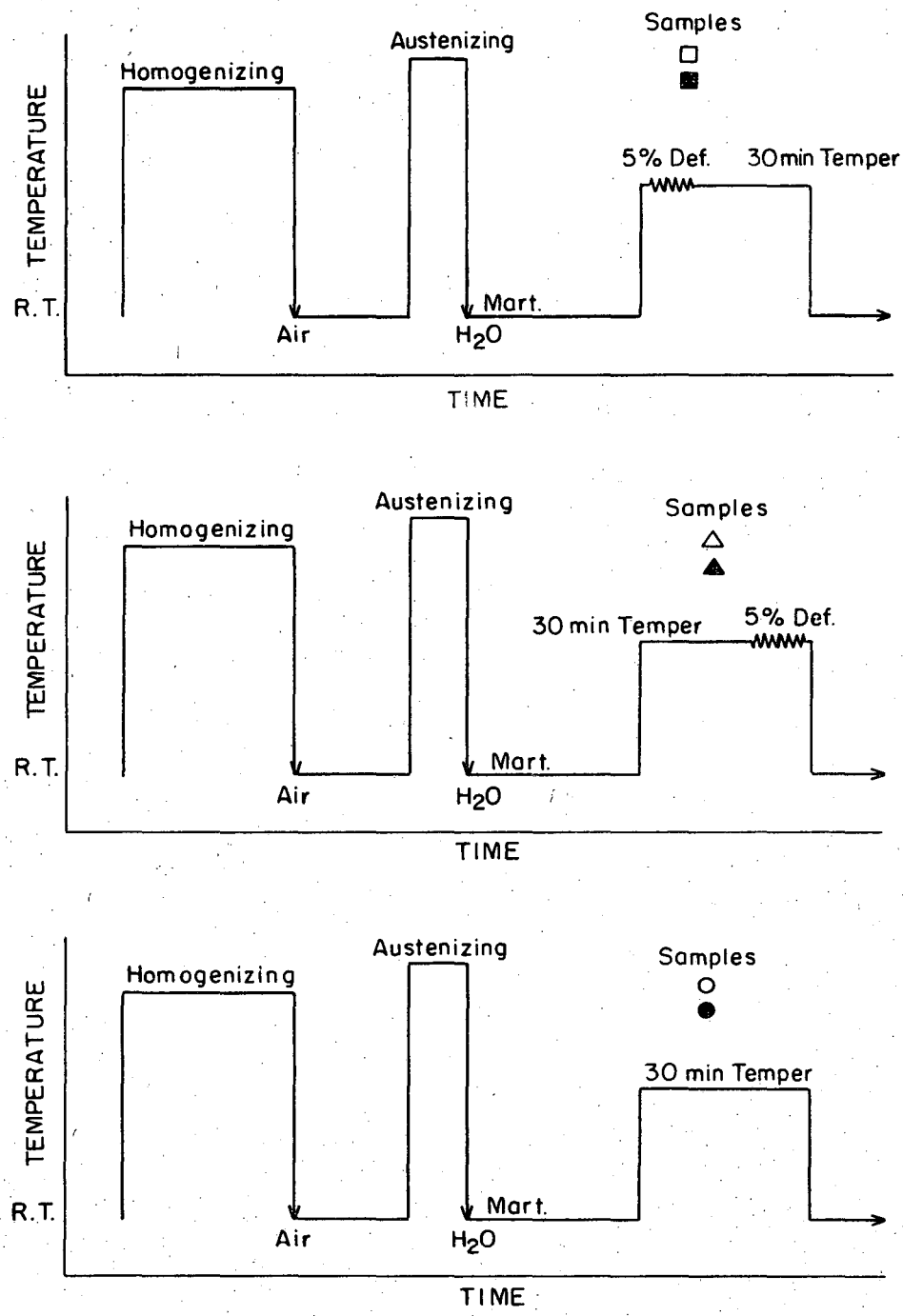

XBL 685-876

Fig. 1 Schematic representation of the thermomechanical treatments.

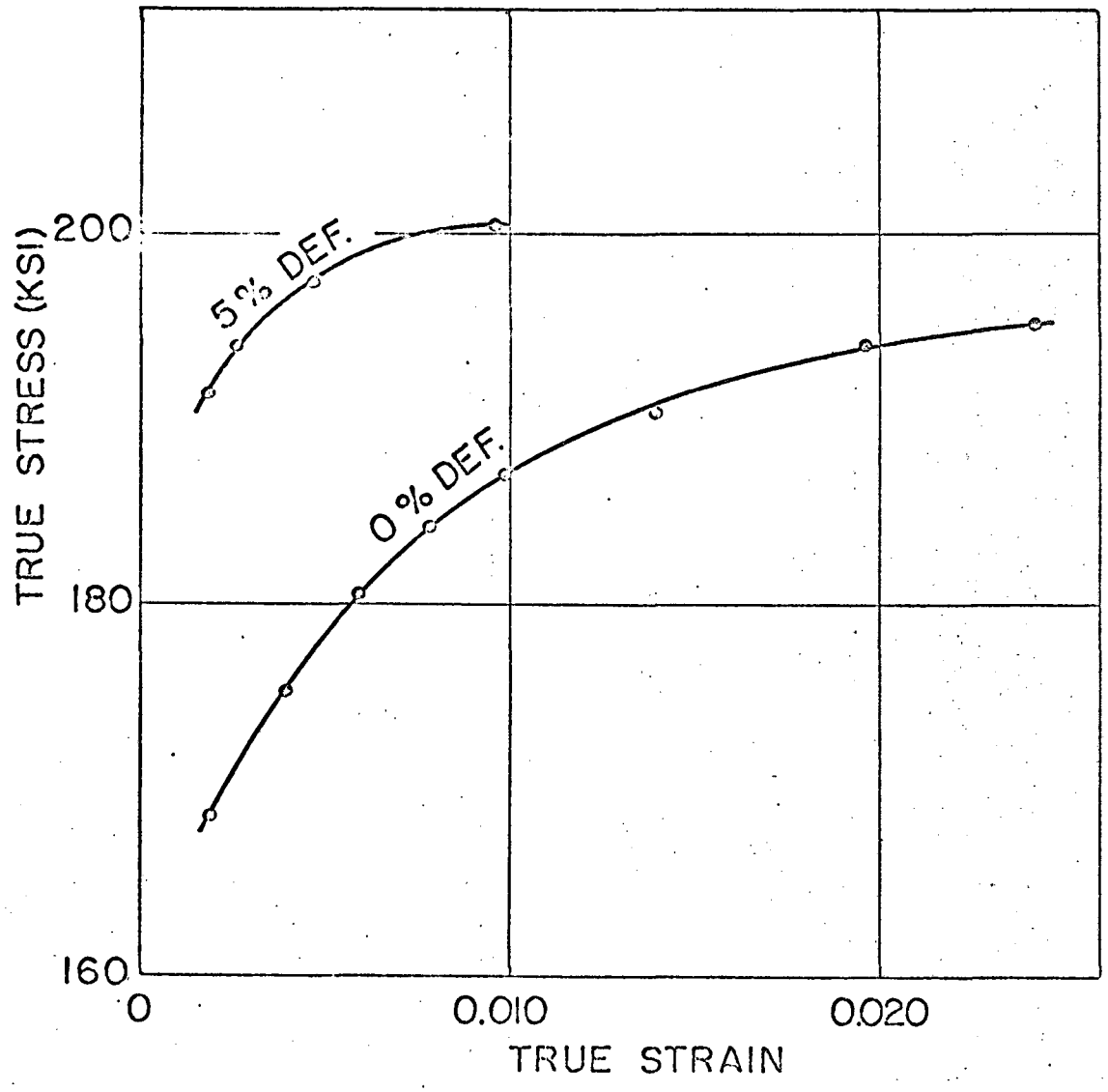

Fig. 2a True stress-true strain curves of Fe-Cr-C steel processed at 25°C.

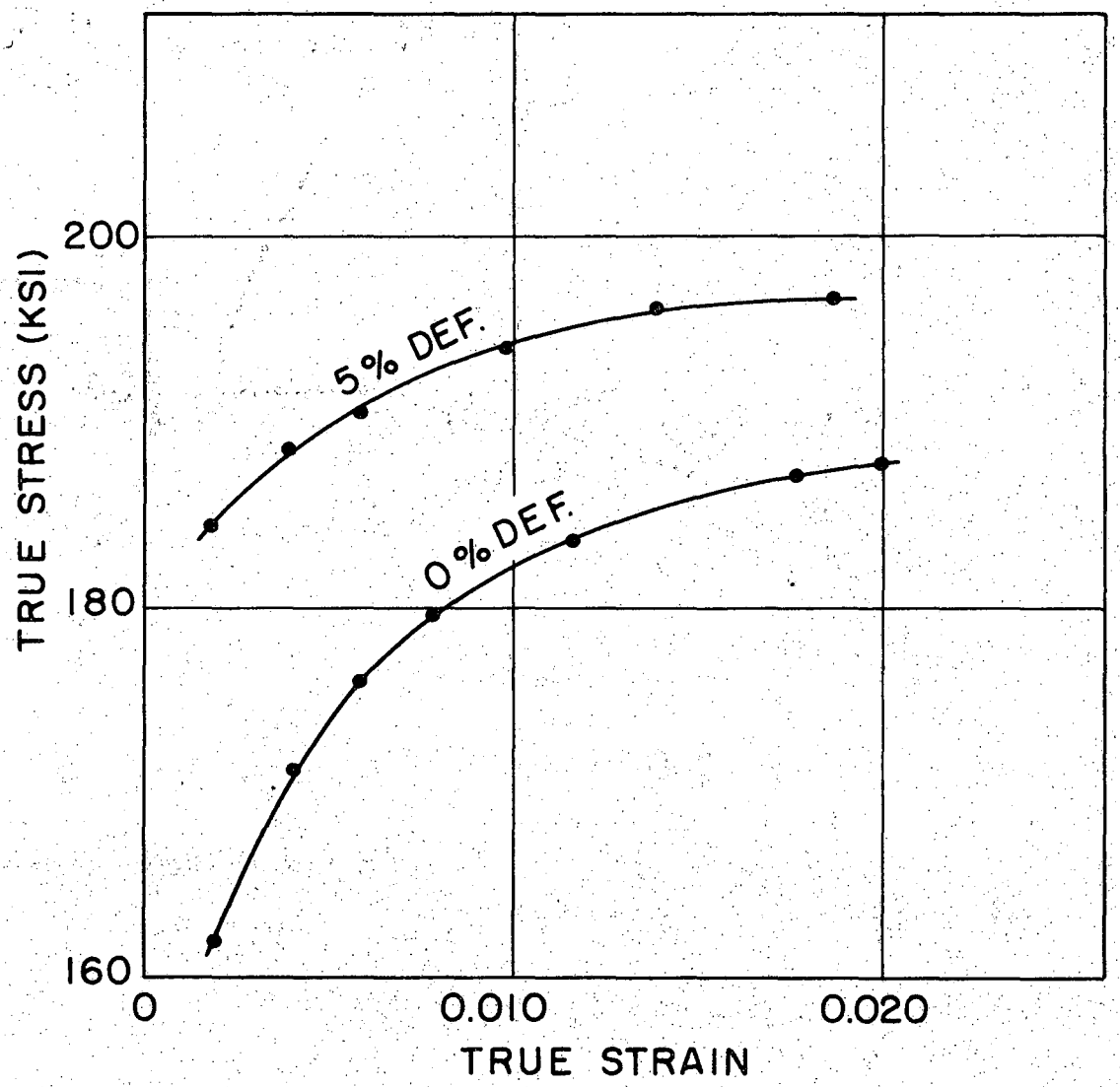

Fig. 2b True stress-true strain curves of Fe-Cr-C steel processed at 250°C.

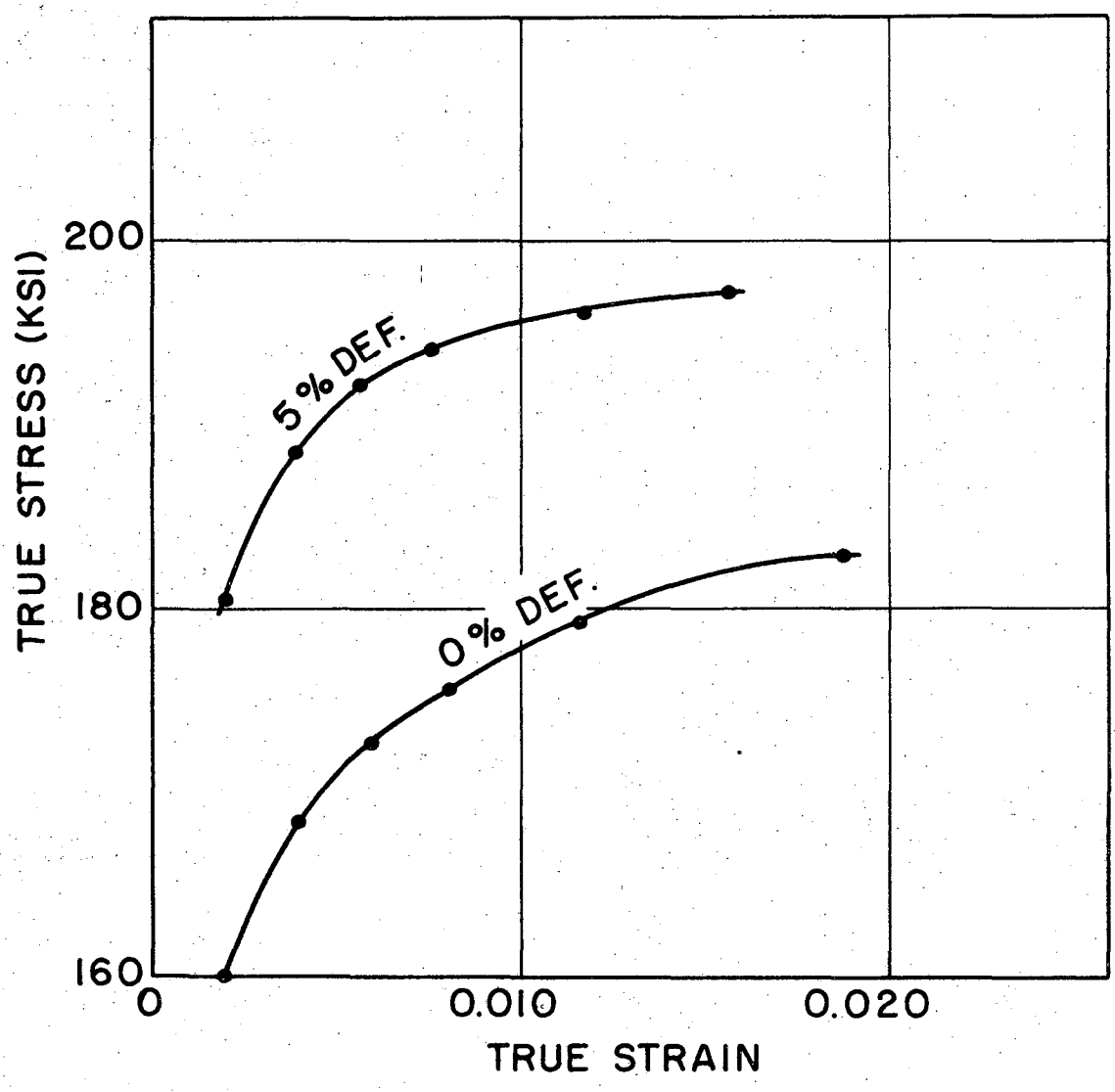

Fig. 2c True stress-true strain curves of Fe-Cr-C steel processed at 375°C.

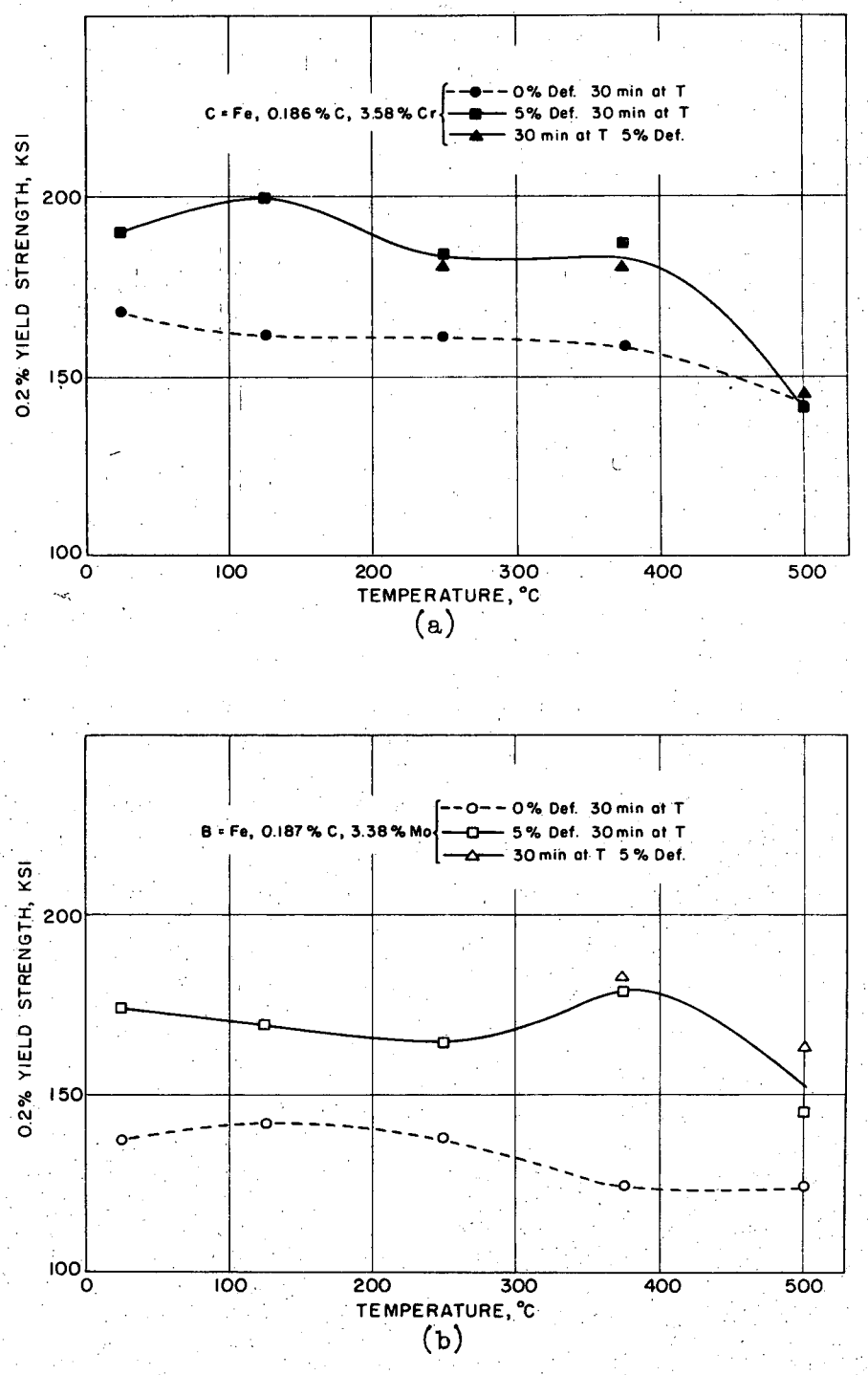

Fig. 3 Effect of dynamic strain aging upon the yield strength of (a) Fe-Cr-C and (b) Fe-Mo-C steels as a function of processing temperature.

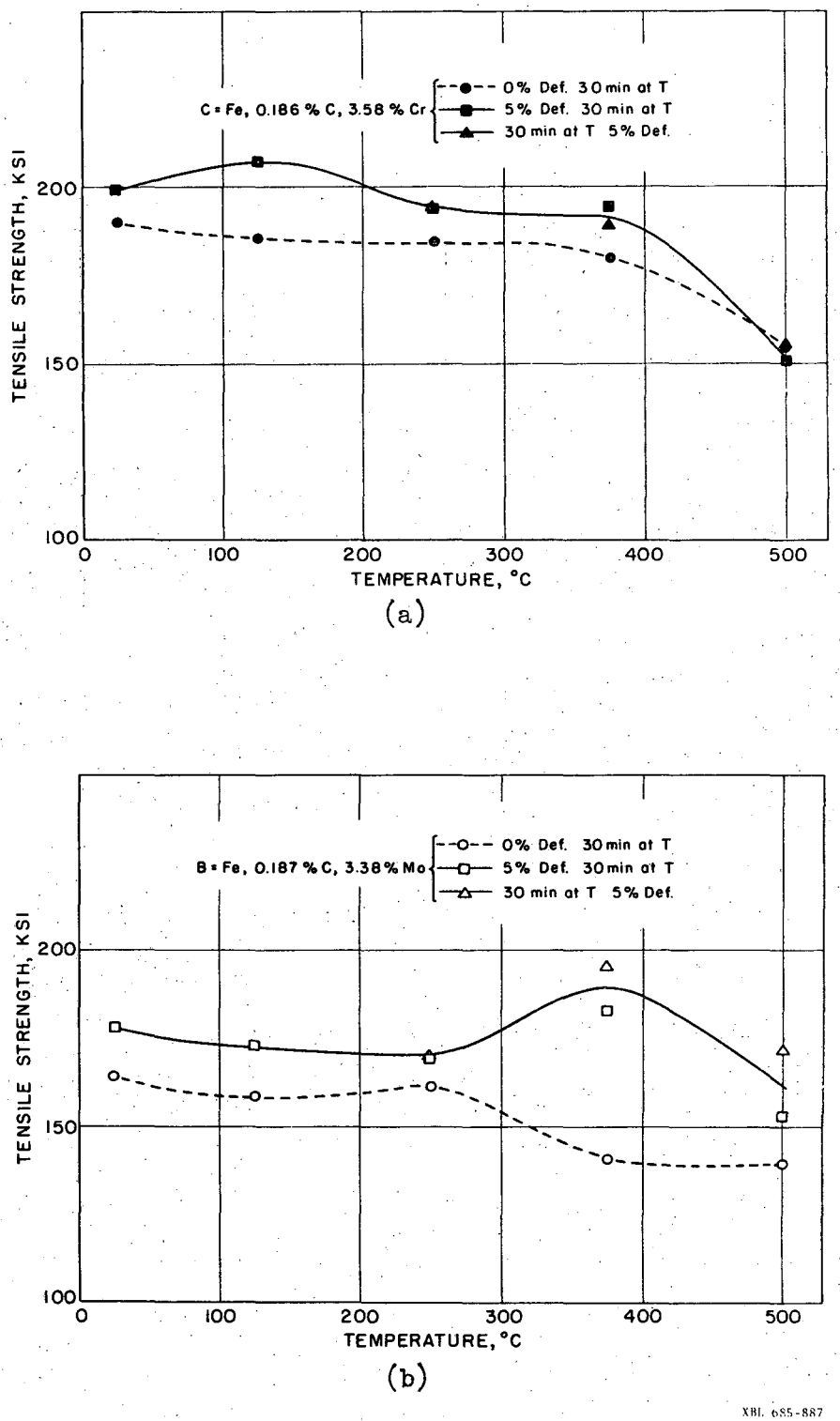

Fig. 4 The effect of dynamic strain aging upon the tensile strength of (a) Fe-Cr-C and (b) Fe-Mo-C steels as a function of processing temperature.

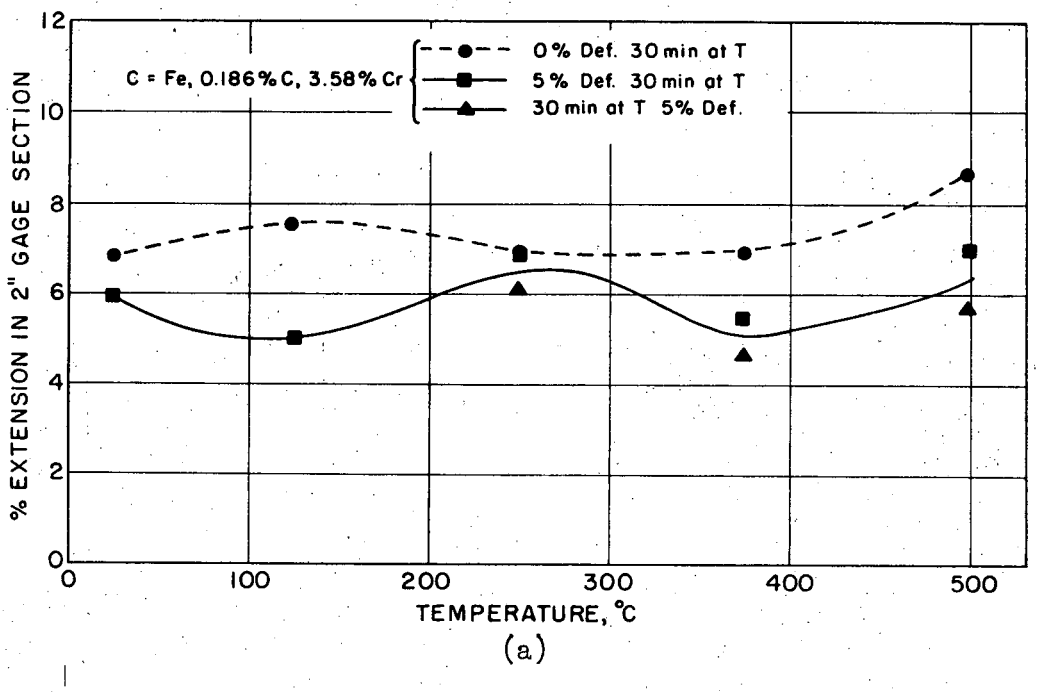

(a)

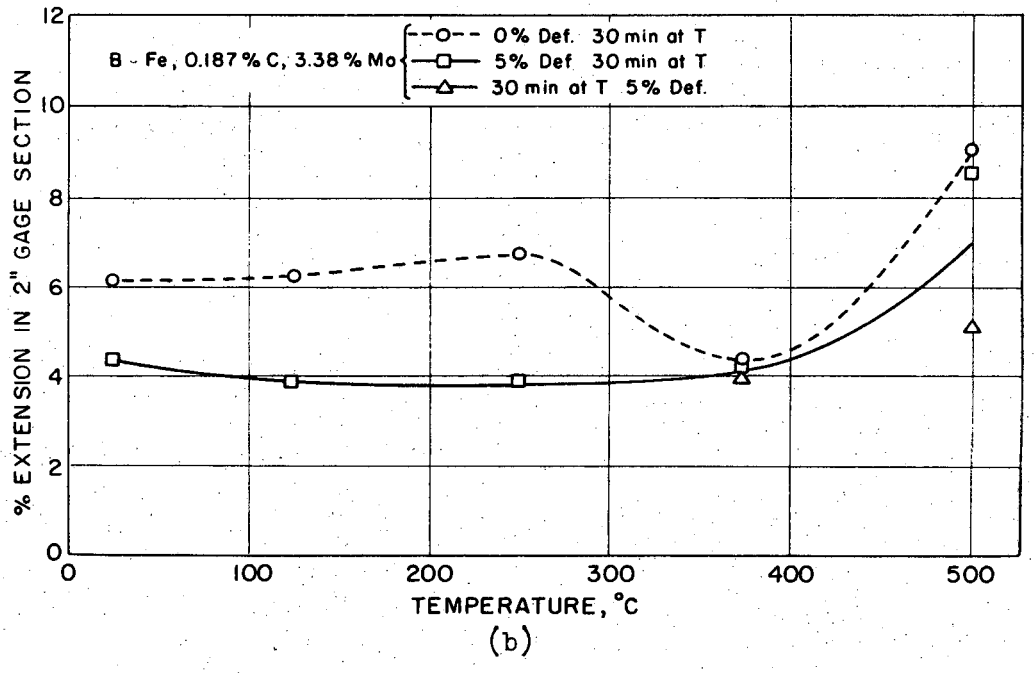

(b)

XBL 685-883

Fig. 5 The effect of dynamic strain aging upon the extension of (a) Fe-Cr-C and (b) Fe-Mo-C steels, as a function of processing temperature.

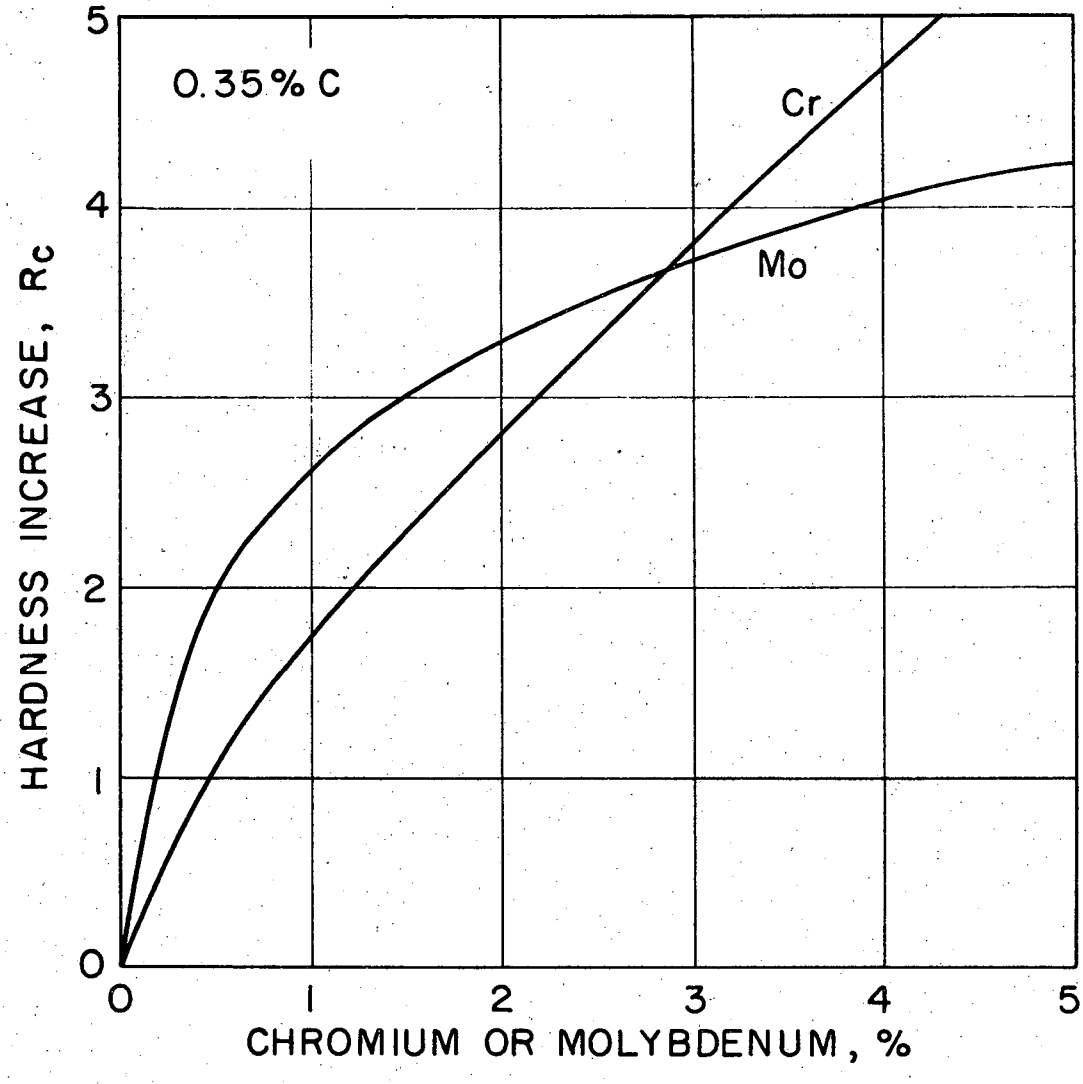

XBL 685-884

Fig. 6 Effect of molybdenum and chromium upon maximum martensitic hardness in 0.35% carbon steels.[17]

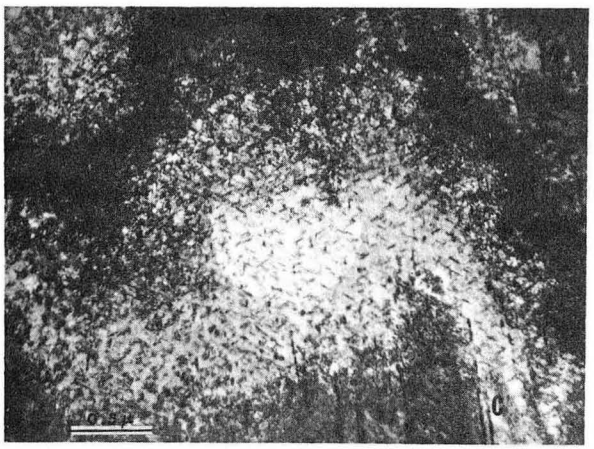

(a)

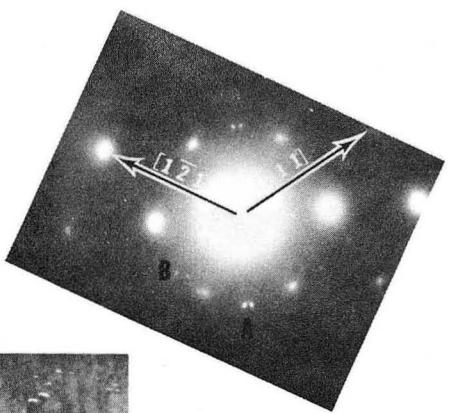

(c)

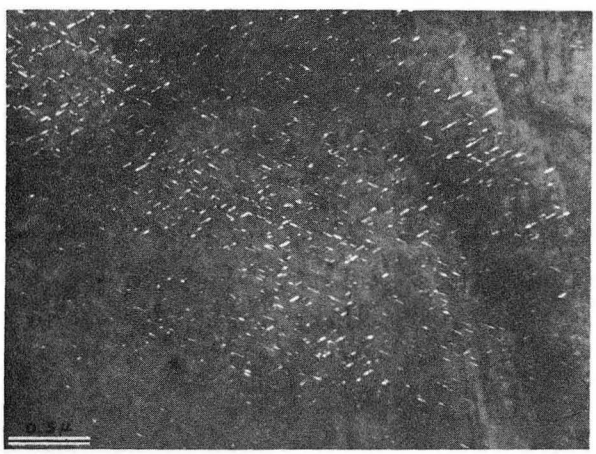

(b)

XBB 685-3023

Fig. 7 Thin foil micrographs of sample 1C; $\langle 111 \rangle_{orient}$.
a) Bright field image revealing Widmenstatten precipitate pattern along $\langle 211 \rangle$ directions, high dislocation density, twinning at "C"
b) Dark field image of (a) due to precipitate spots at "A" in (c)
c) Select area diffraction with precipitate spots at "A", streaking of spots at "B"

(a)

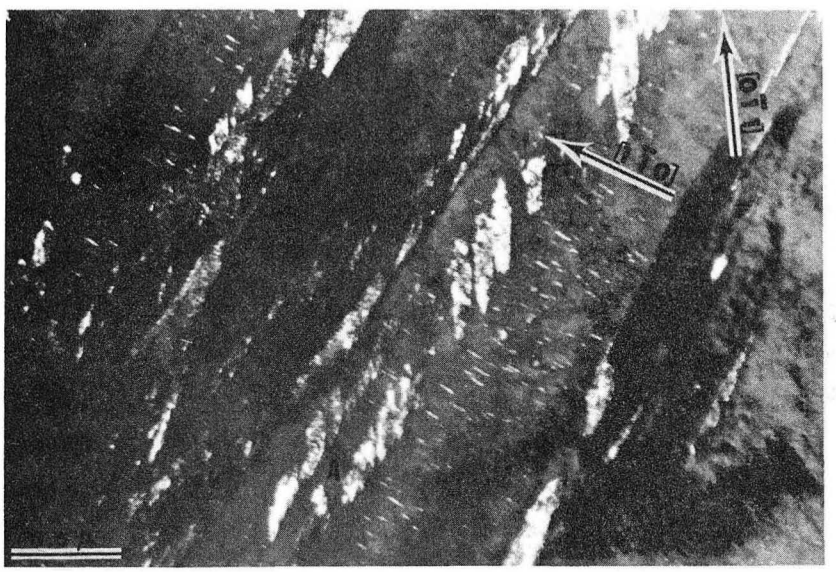

(b)

XBB 685-3009

Fig. 8 Thin foil micrograph of sample 2C; $\langle 111 \rangle_{orient}$.
a) Bright field image showing precipitates along $\langle 110 \rangle$ directions, high dislocation density, twins at "A"
b) Dark field image of (a) revealing precipitates, twins at "A"

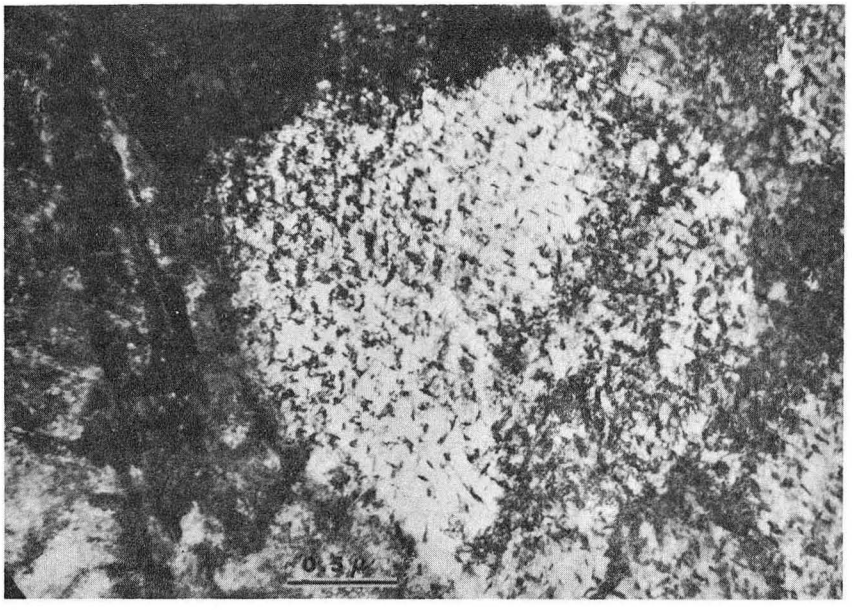

(a)

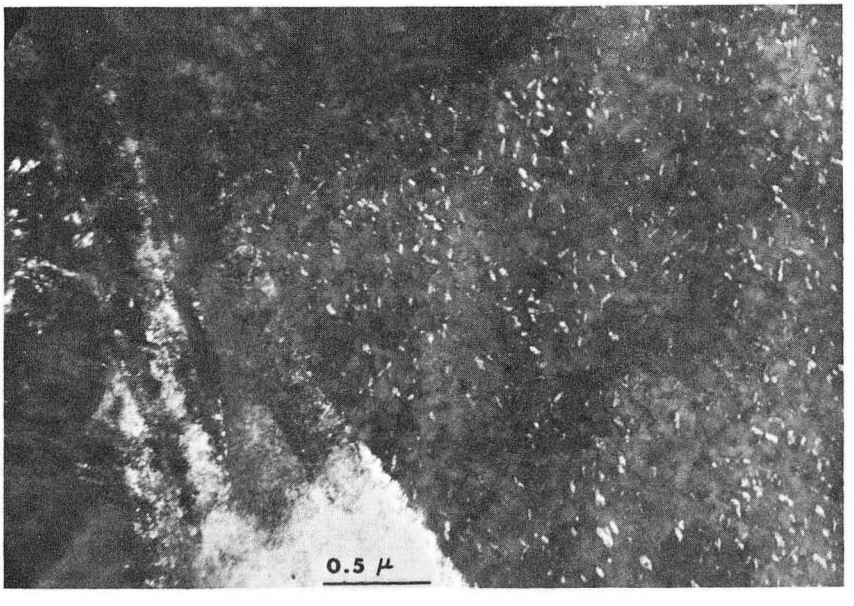

(b)

XBB 685-3011

Fig. 9 Thin foil micrographs of sample 3C; $\langle 311 \rangle_{orient}$

a) Bright field image showing distorted precipitates

b) Dark field image of (a) showing distorted precipitates

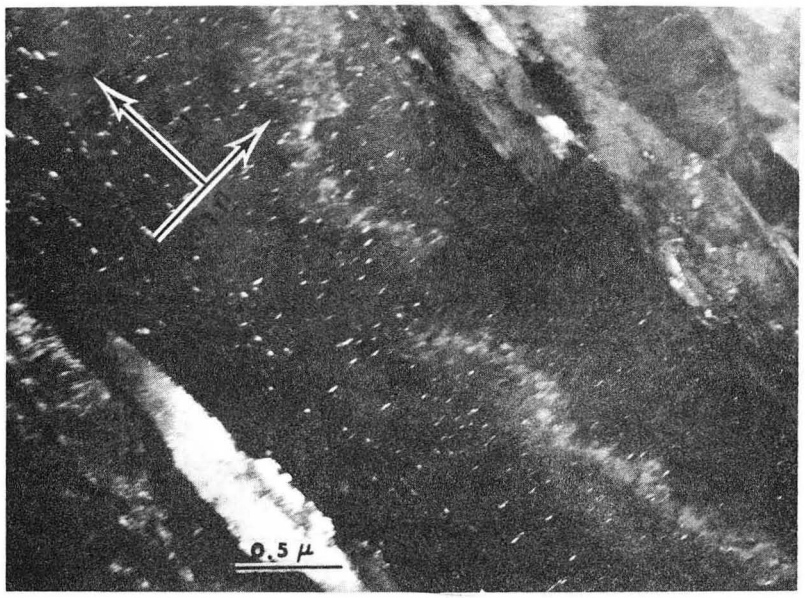

(a)

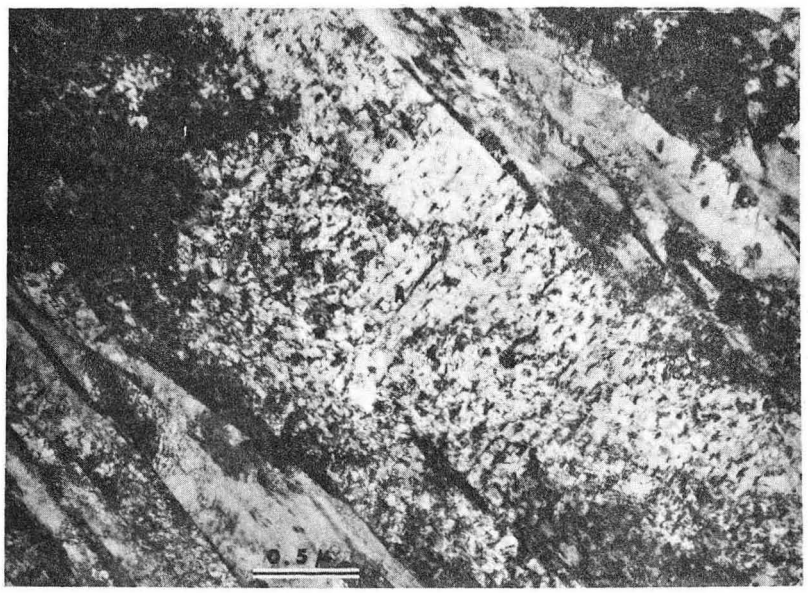

(b) XBB 685-3029

Fig. 10 Thin foil micrographs of sample 10C; $\langle 100 \rangle_{orient}$

a) Dark field image of (b) showing precipitate along $\langle 110 \rangle$ directions.

b) Bright field image revealing precipitates and dislocation contrast at "A"

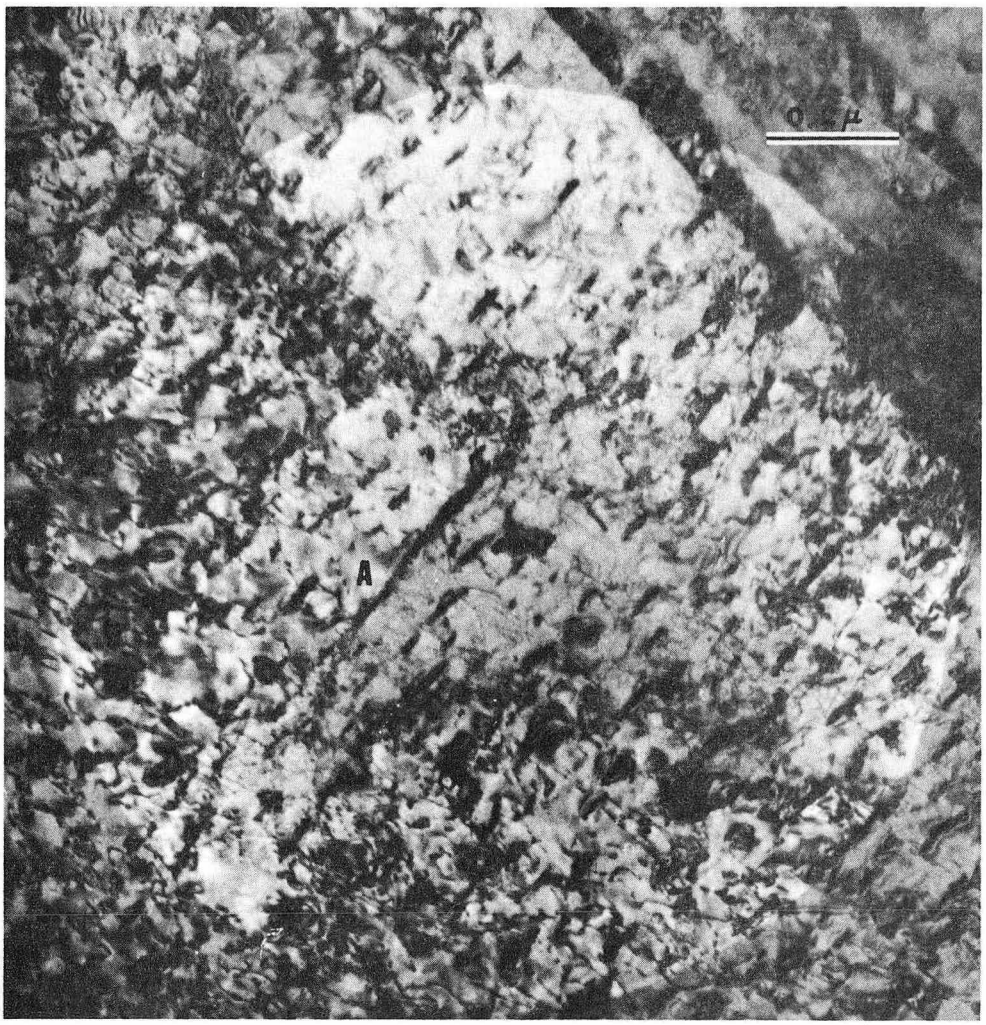

XBB 685-3014

Fig. 11 Thin foil micrograph of sample 10C; $\langle 100 \rangle_{orient}$
Bright field image enlargement of Fig. 10b showing dislocation contrast of "A"

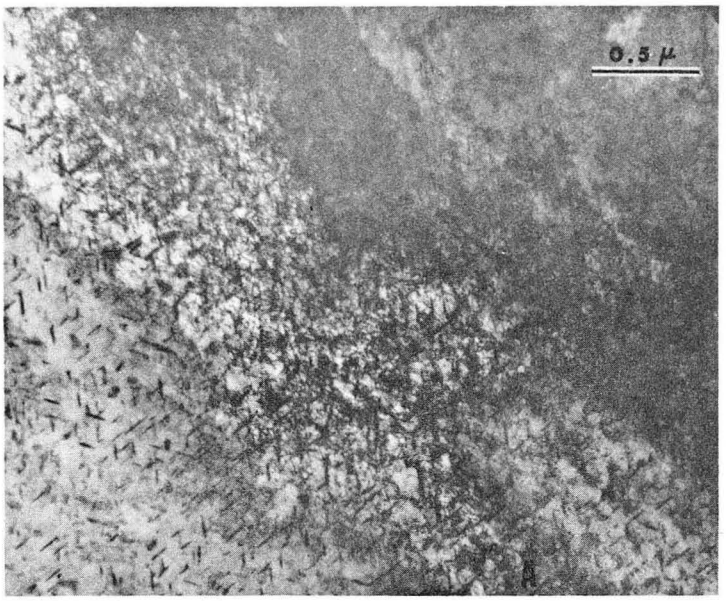

(a)

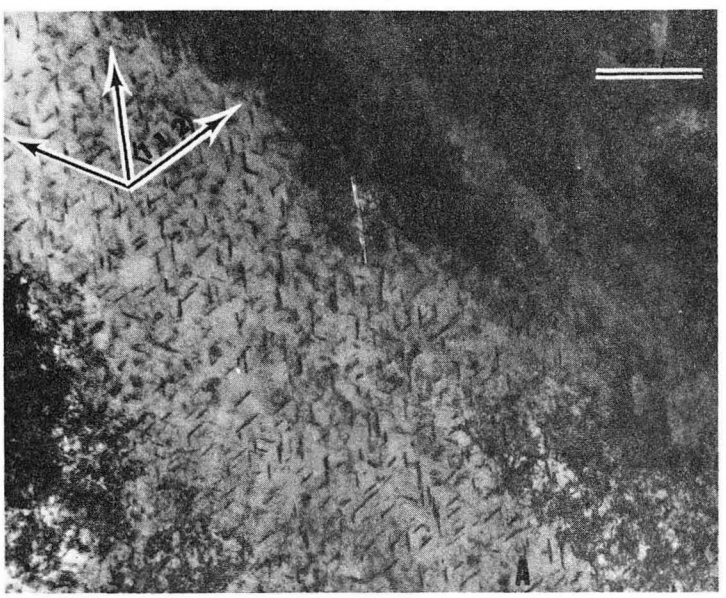

(b)

XBB 685-3012

Fig. 12 Thin foil micrographs of sample 8C; $\langle 111 \rangle_{orient}$

a) Bright field image showing high dislocation density, Widmanstatten precipitate pattern along $\langle 211 \rangle$ directions.

b) Bright field image showing same area as (a) but tilted slightly. Note change in dislocation contrast of "A".

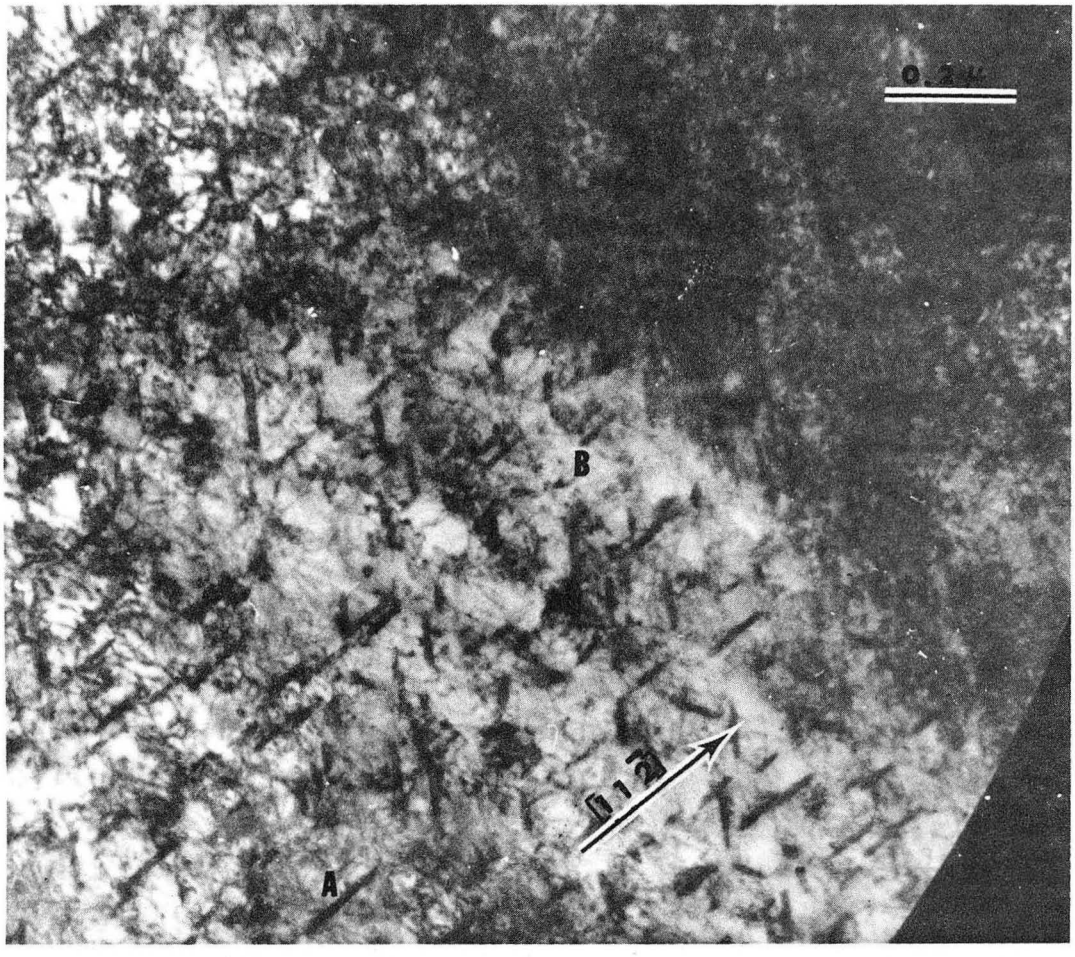

XBB 685-3017

Fig. 13 Thin foil micrograph of sample 8C; $\langle 111 \rangle_{orient}$
Bright field image enlargement of Fig. 12b with "A" indicating same area in both figures. Note small round precipitates at "B"

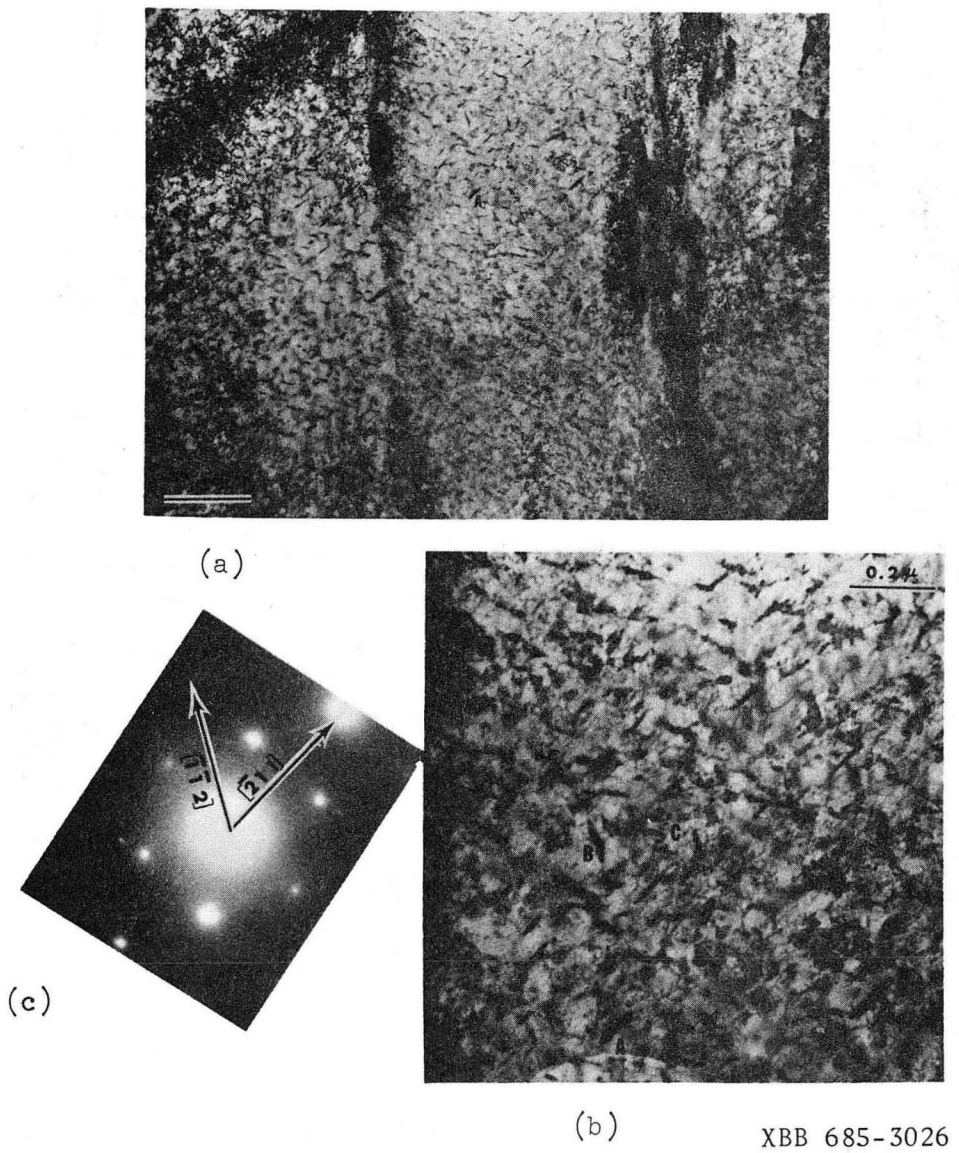

Fig. 14 Thin foil micrographs of sample 9C; $\langle 111 \rangle_{orient}$

a) Bright field image showing precipitates at "A"

b) Bright field image enlargement of (a) showing same area as (a) at "A", but precipitates at "B", small round precipitates at "C"

c) Selected area diffraction indicating precipitates lie along $\langle 211 \rangle$ directions.

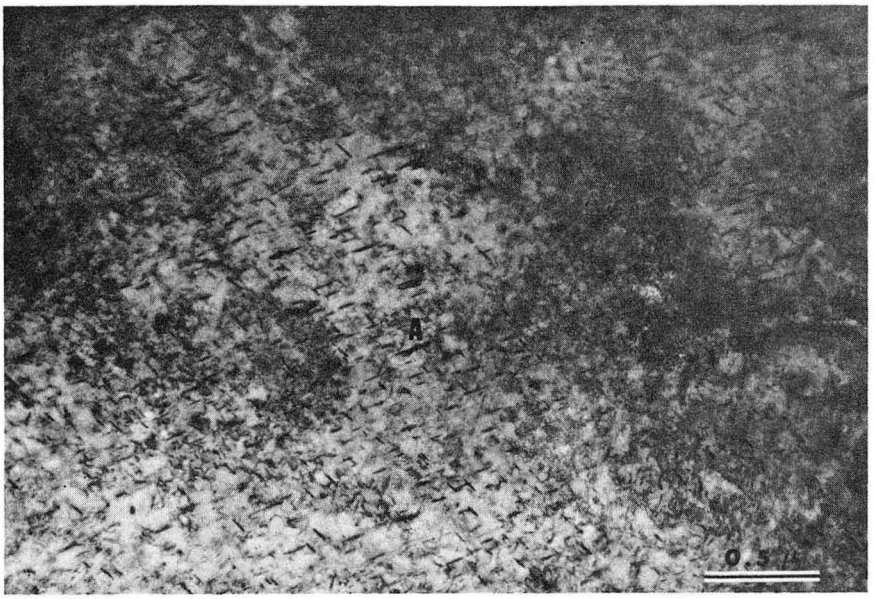

(a)

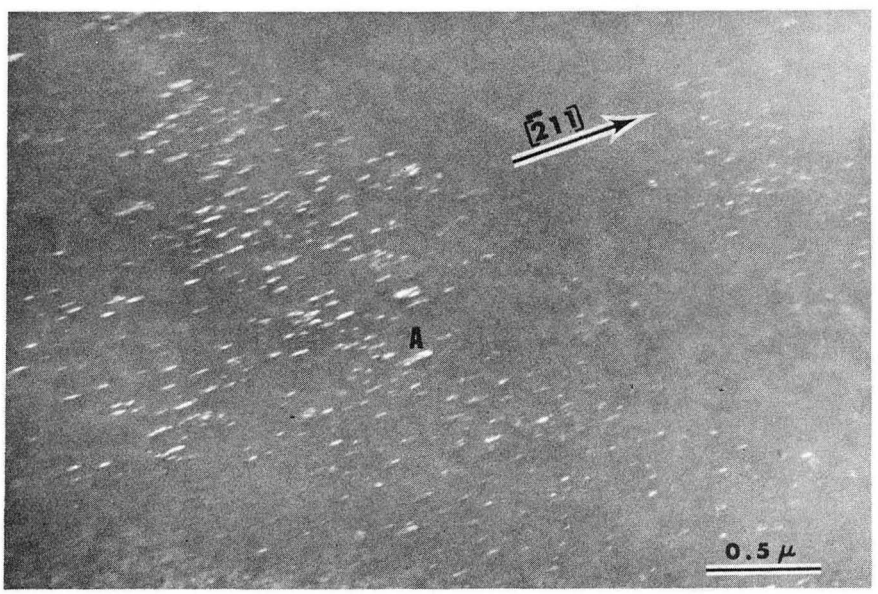

(b) XBB 685-3008

Fig. 15 Thin foil micrographs of sample 9C; $\langle 111 \rangle_{orient}$

a) Bright field image showing Widmanstatten precipitate pattern at "A"

b) Dark field image of (a) showing precipitates at "A" lie along [2̄11] direction

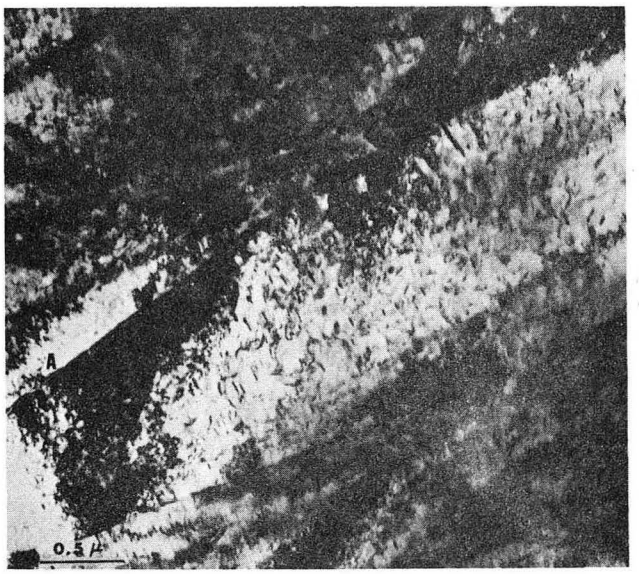

(a)

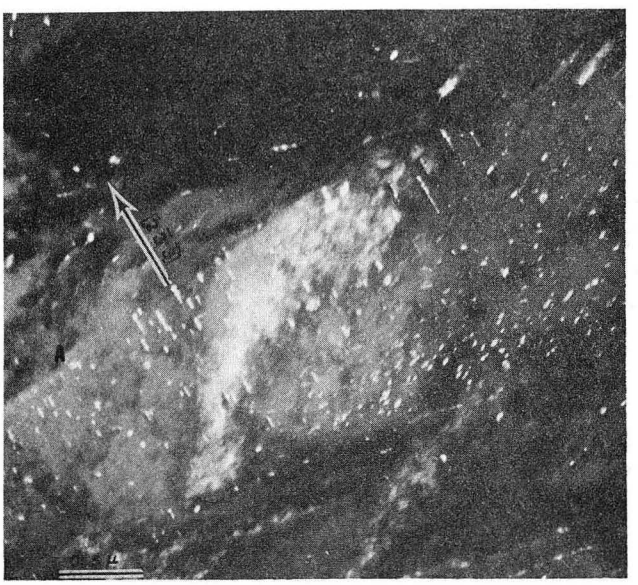

(b) XBB 685-3025

Fig. 16 Thin foil micrographs of sample 13C; $\langle 311 \rangle_{orient}$

a) Bright field image revealing precipitates, recrystallization at "A"

b) Dark field image of (a) showing precipitates along $[2\bar{3}\bar{3}]$ direction, grain boundary at "A"

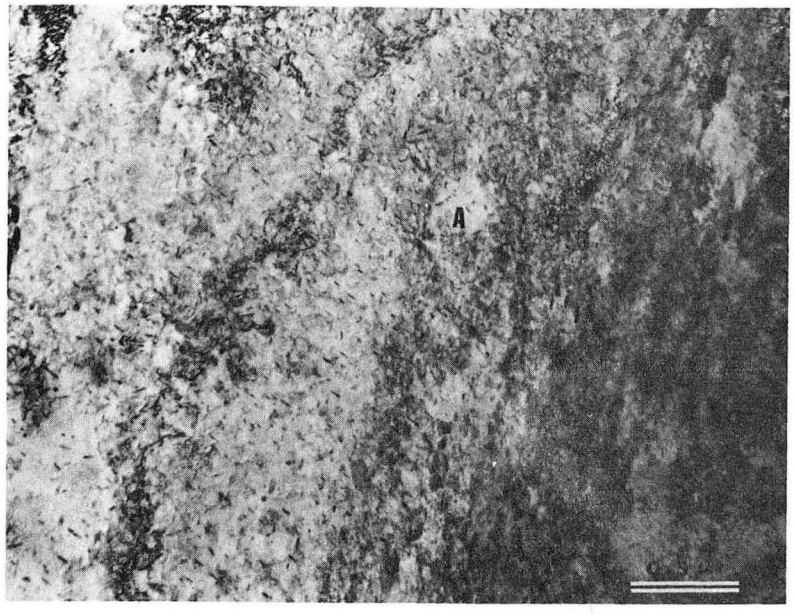

(a)

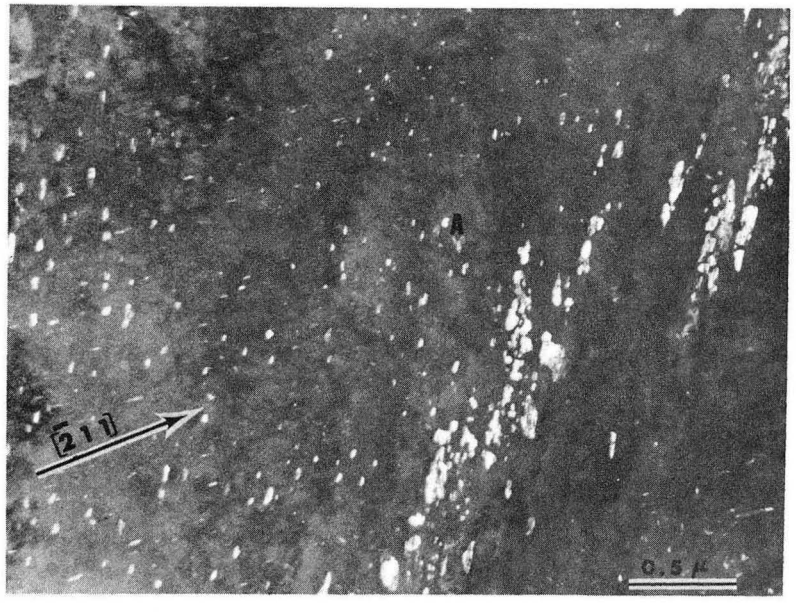

(b)

XBB 685-3013

Fig. 17 Thin foil micrographs of sample 11C; $\langle 111 \rangle_{orient}$

a) Bright field image showing dissolution of precipitates at "A"

b) Dark field image of (a) showing some precipitates along [$\bar{2}$11], spherodizing and dissolution of precipitates at same "A" as in (a) with very small precipitates to right of "A"

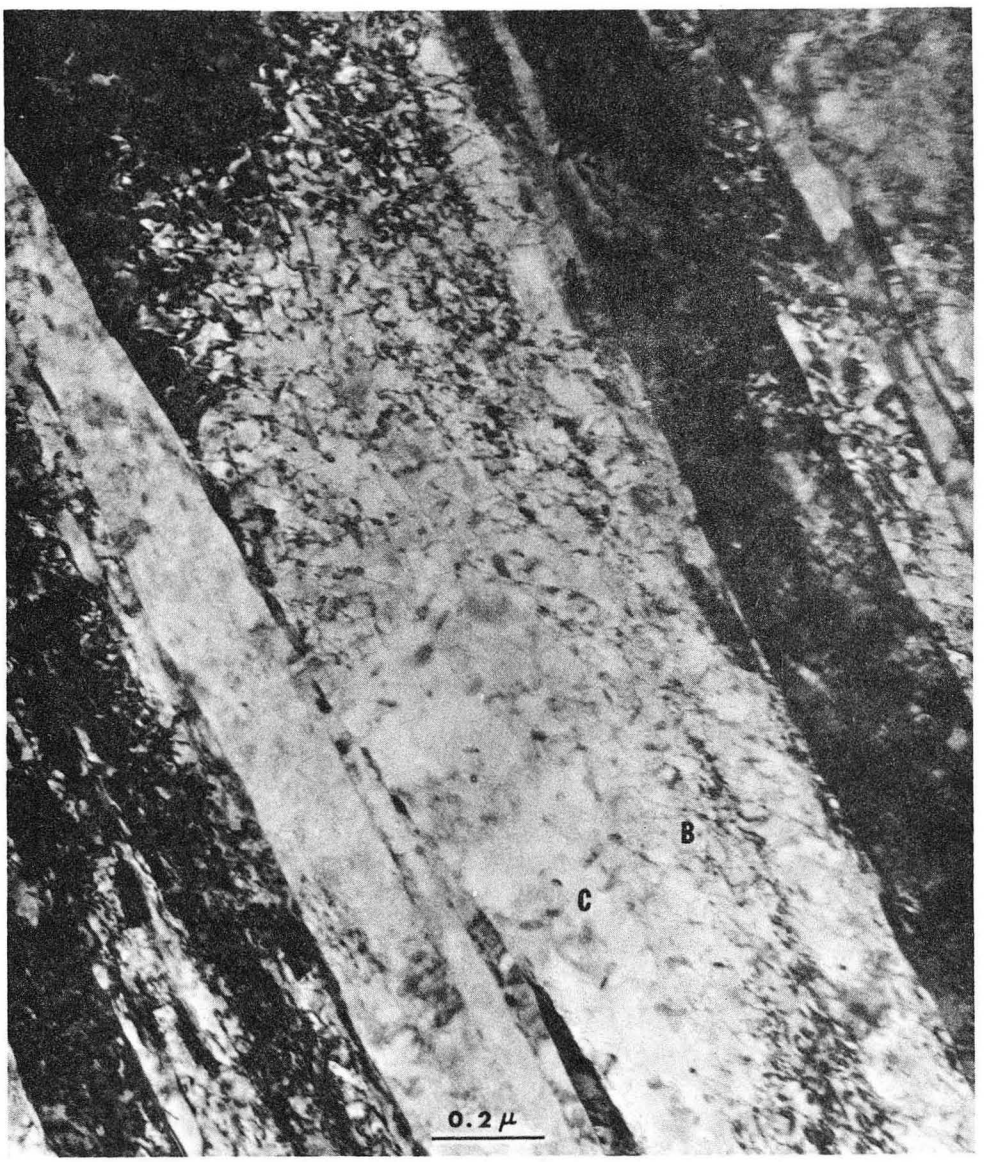

XBB 685-3010

Fig. 18 Thin foil micrograph of sample 11C; $\langle 111 \rangle_{orient}$
Bright field image showing recrystallization at "A", precipitation on dislocations at "B", dissolution of precipitates at "C"

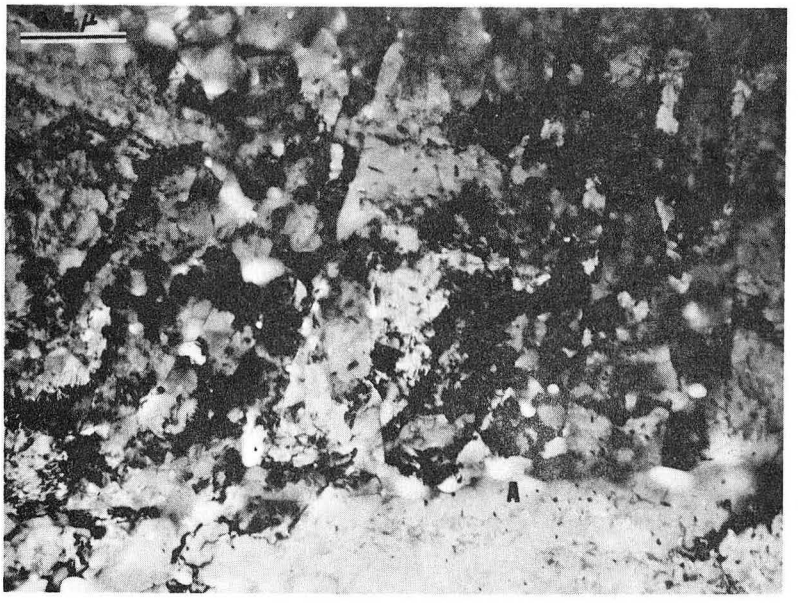

(a)

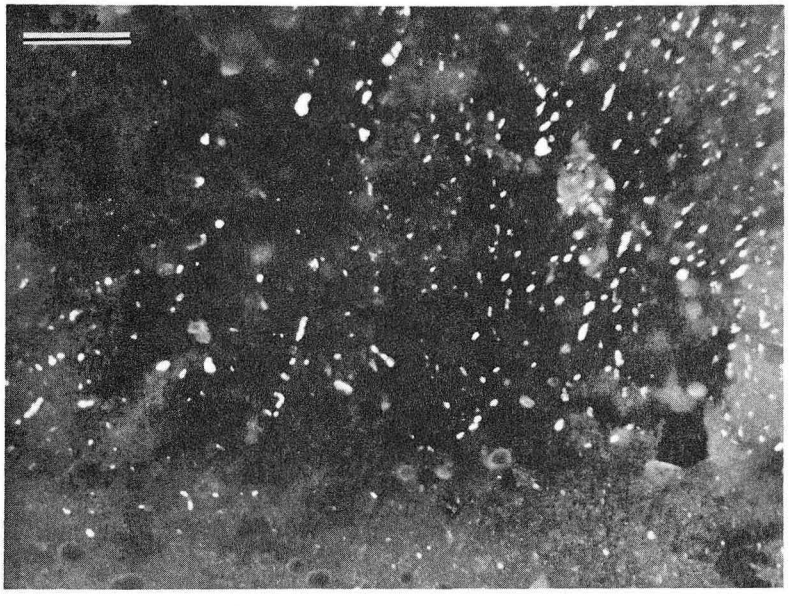

(b) XBB 685-3030

Fig. 19 Thin foil micrographs of sample 13C*; $\langle 311 \rangle_{orient}$

a) Bright field image showing spherodized precipitate and recrystallization at "A"

b) Dark field image of (a) showing spherodized precipitates, an addition very fine precipitates near "A"

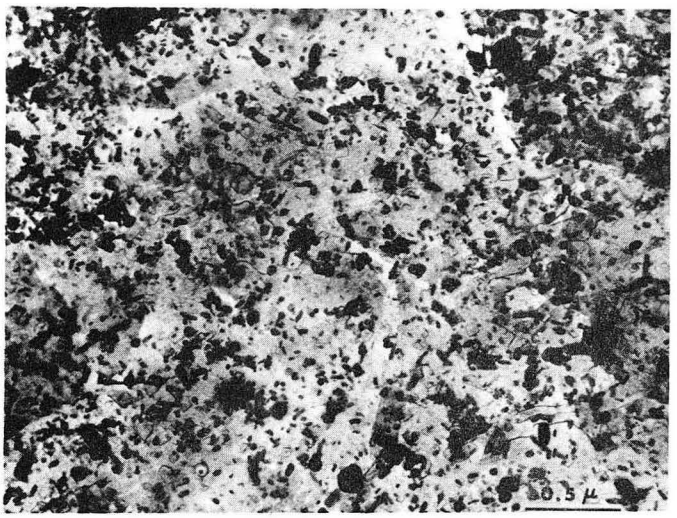

(a)

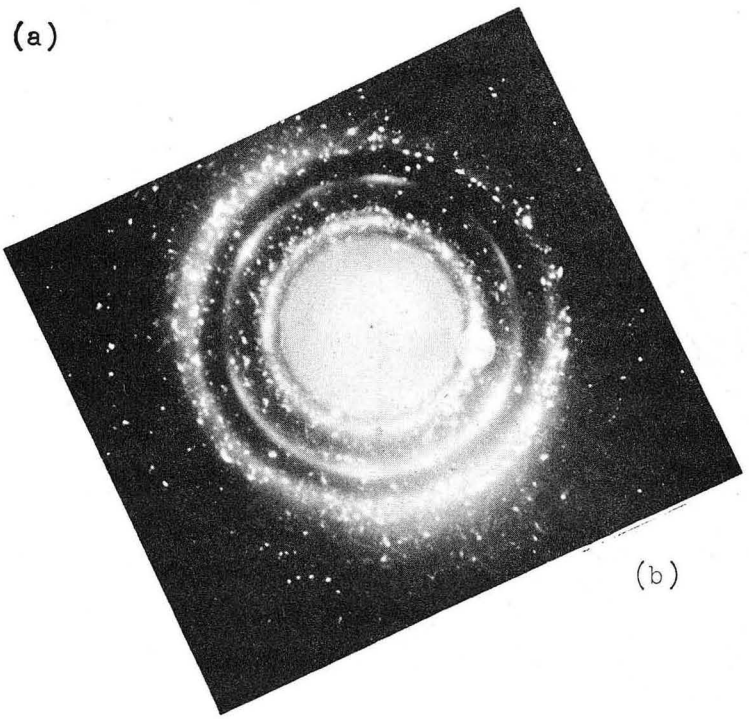

(b)

XBB 685-3027

Fig. 20 Carbon extraction replica of sample 13C*
(a) Bright field image showing precipitates
(b) Selected area diffraction showing streaking of precipitates spots in ring pattern

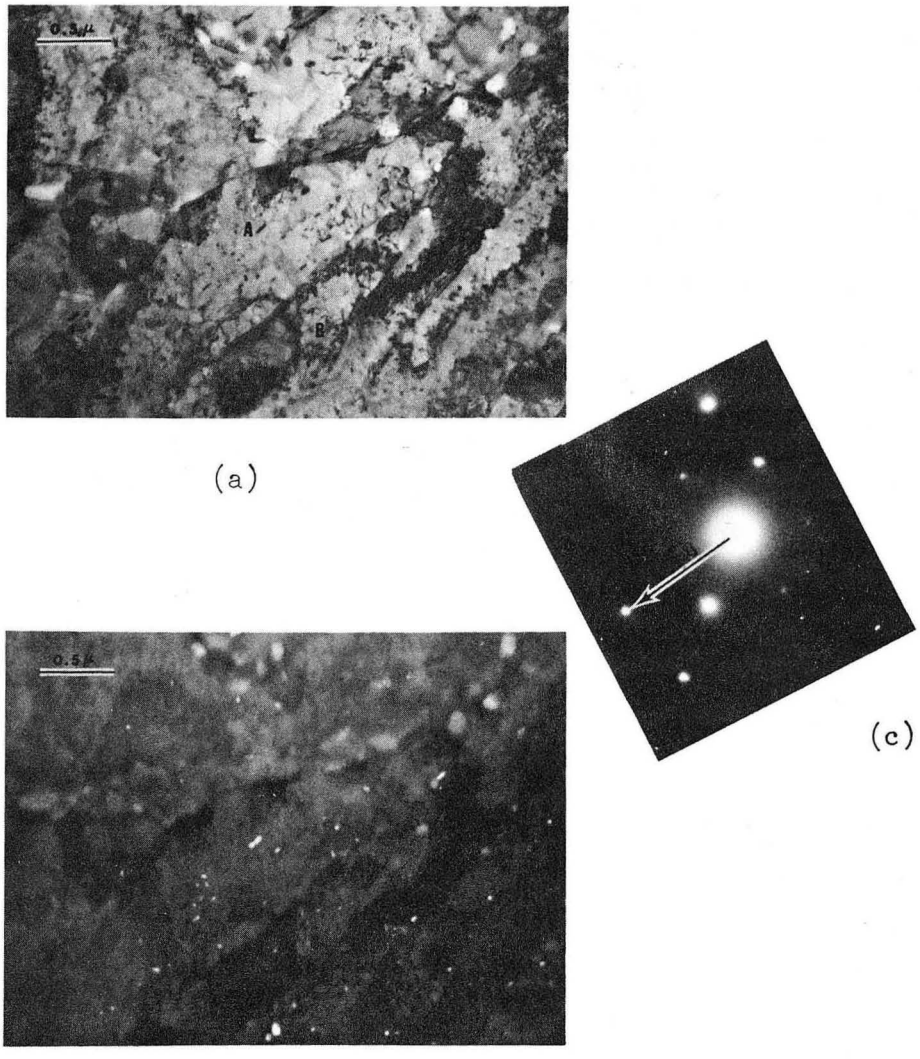

Fig. 21 Thin foil micrographs of sample 11C*; $\langle 111 \rangle_{orient}$
(a) Bright field image showing recrystallization dislocation at "A", precipitates on dislocations at "B"
(b) Dark field image of (a) showing precipitates at B due to precipitate spot at "C" in (c)
(c) Selected area diffraction indicating $[2\bar{1}\bar{1}]$ direction, precipitate spot at "C"

XBB 685-3007

Fig. 22 Thin foil micrograph of sample 11C*; $\langle 111 \rangle_{orient}$
Bright field image showing subgrain formation during recrystallization of "A", spherodized precipitates and precipitation on dislocation near "B", polygonization at "C"

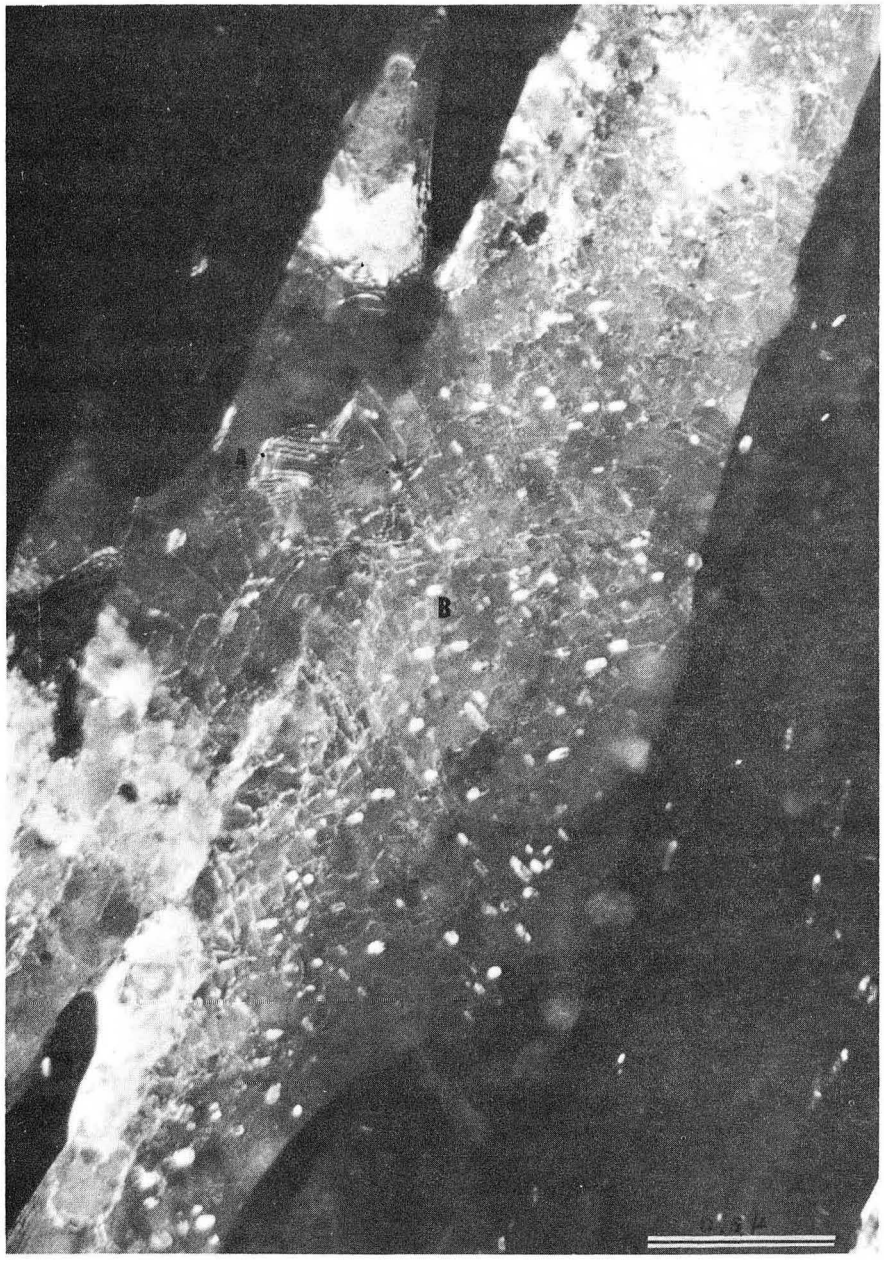

XBB 685-3028

Fig. 23 Thin foil micrograph of sample 11C*; $\langle 111 \rangle_{orient}$
Dark field image of Fig. 22 with subgrain formation at "A" spherodized precipitate and precipitation on dislocations at "B"

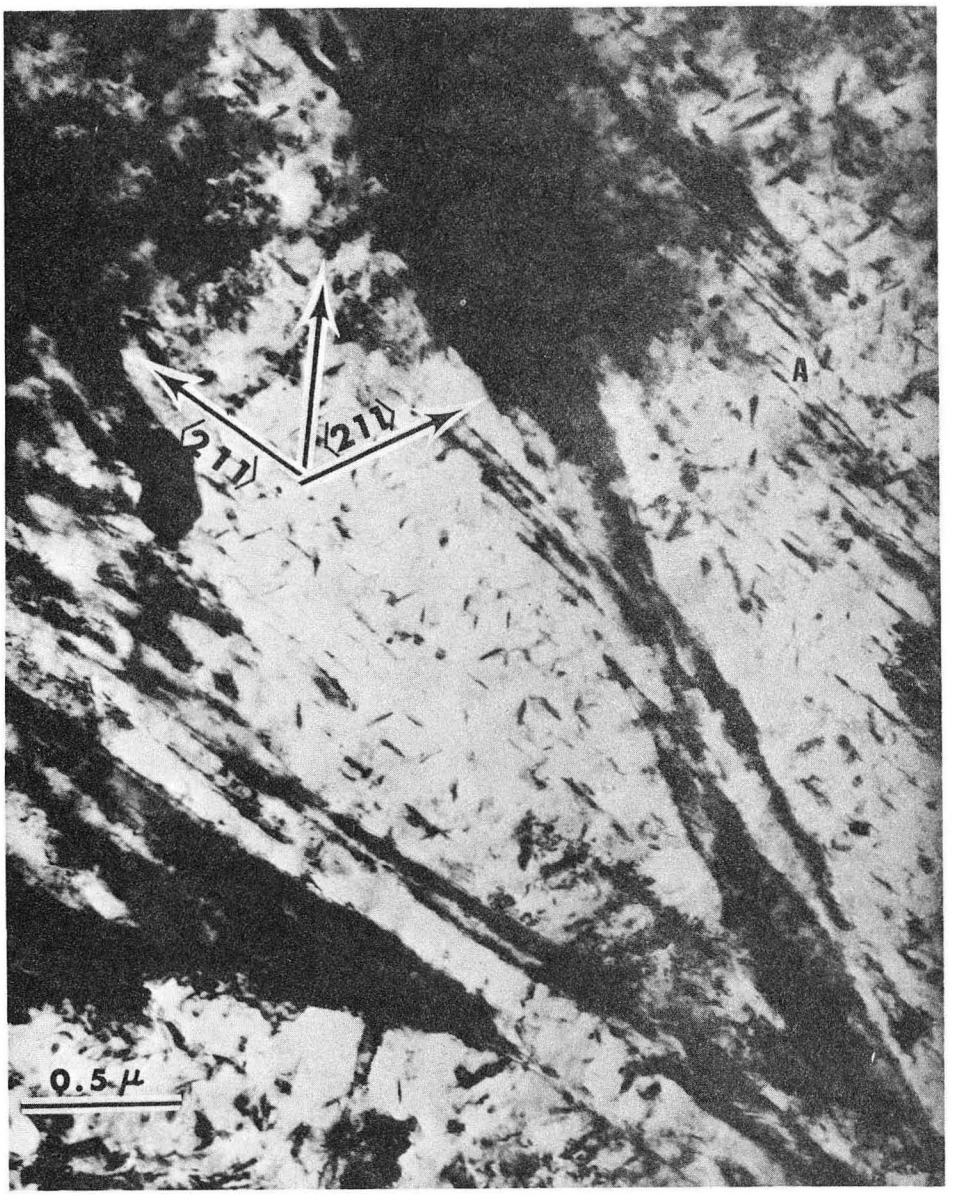

XBB 685-3024

Fig. 24 Thin foil micrograph of sample 1B; $\langle 111 \rangle_{orient}$
Bright field image showing Widmanstatten precipitates along ⟨211⟩ directions, twins at "A"

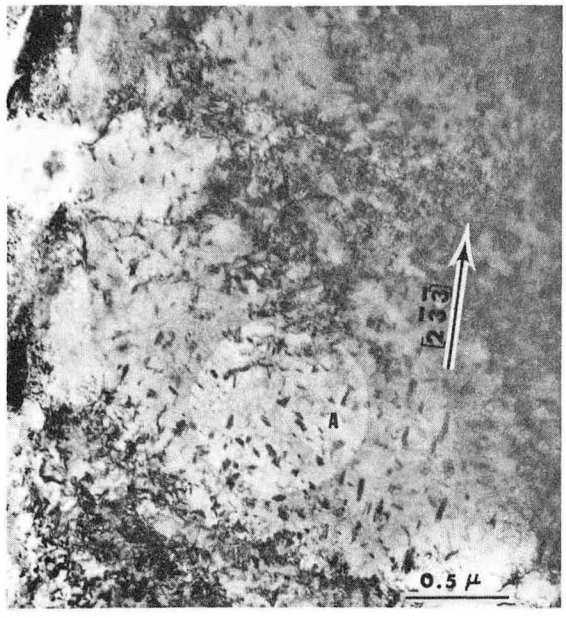

(a)

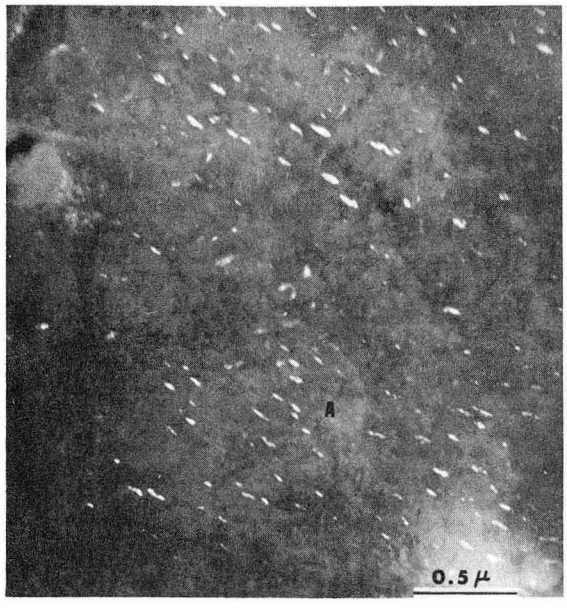

(b)

XBB 685-3020

Fig. 25 Thin foil micrographs of sample 10B; $\langle 311 \rangle_{orient}$

a) Bright field image showing precipitates along $[2\bar{3}\bar{3}]$ direction, dislocations at "A"

b) Dark field image of (a) with precipitates near "A"

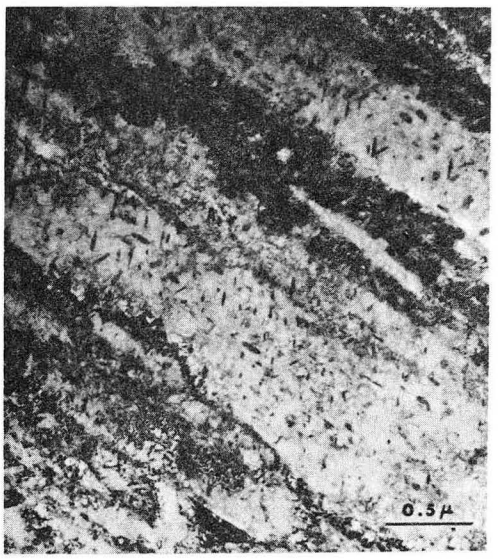

(a)

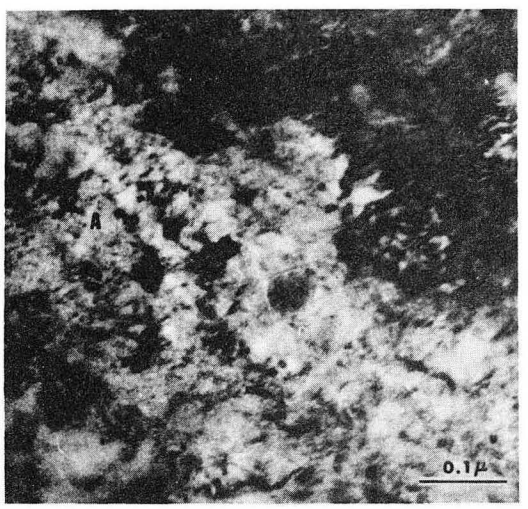

(b)

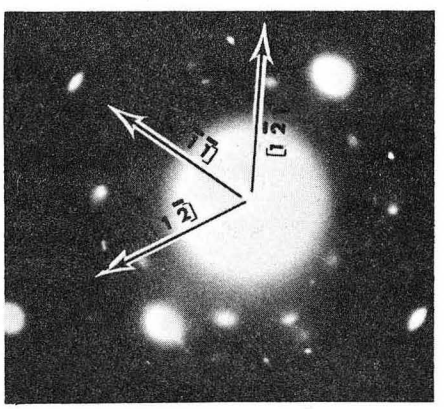

(c)

XBB 685-3016

Fig. 26 Thin foil micrographs of sample 8C; $\langle 111 \rangle_{orient}$

a) Bright field image showing spherodization and dissolution of precipitates, small precipitates near "A"

b) Bright field image enlargement of (a) showing small precipitates near "A"

c) Selected area diffraction indicating $\langle 211 \rangle$ precipitate directions, streaking of precipitate spots at "B"

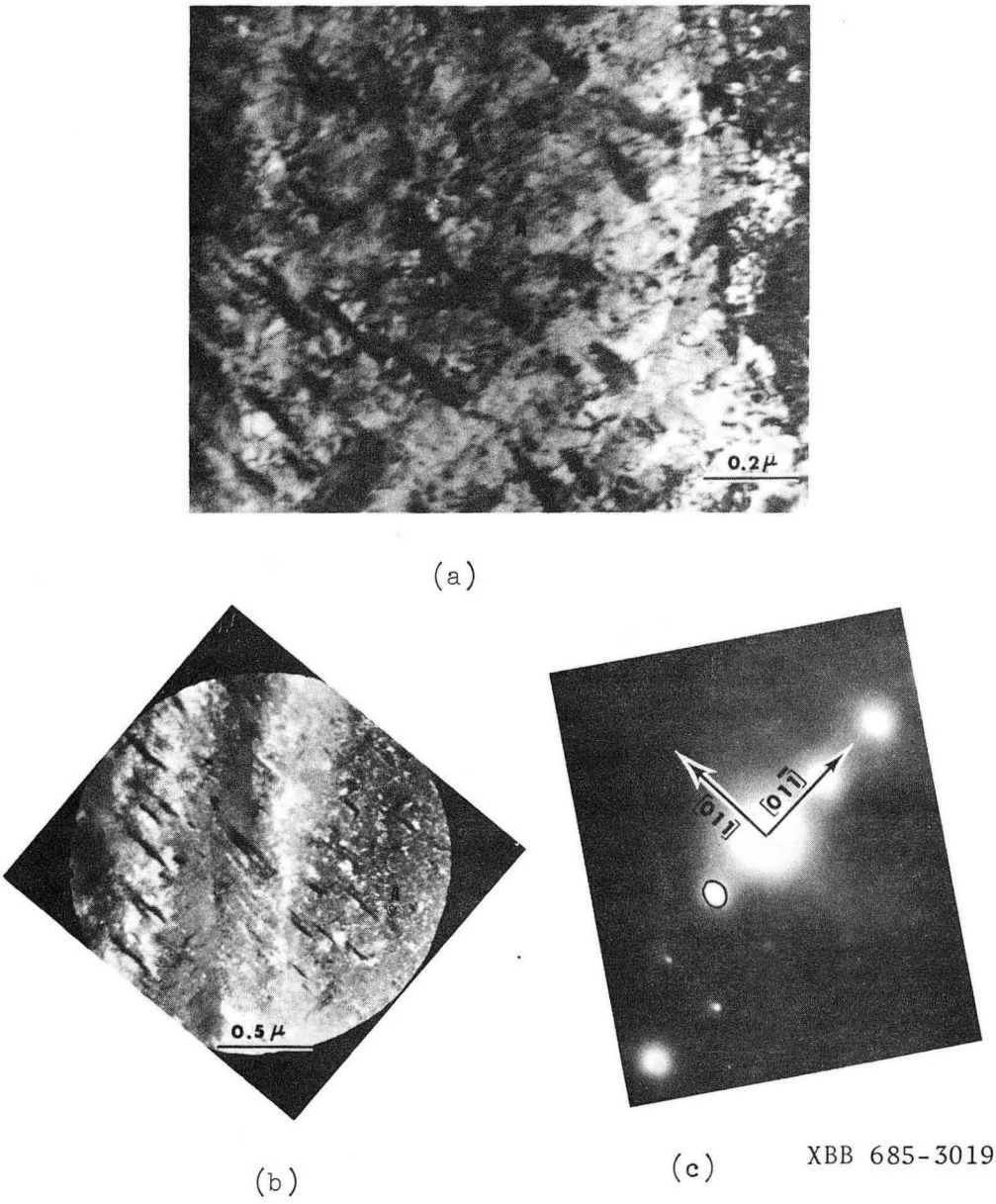

Fig. 27 Thin foil micrographs of sample 8C;[18] $\langle 100 \rangle_{orient}$

a) Enlarged bright field image showing small precipitates on dislocation at "A"
b) Dark field image of (a) showing precipitates on dislocation at "A"
c) Selected area diffraction indicating $\langle 110 \rangle$ directions of large precipitates in (a)

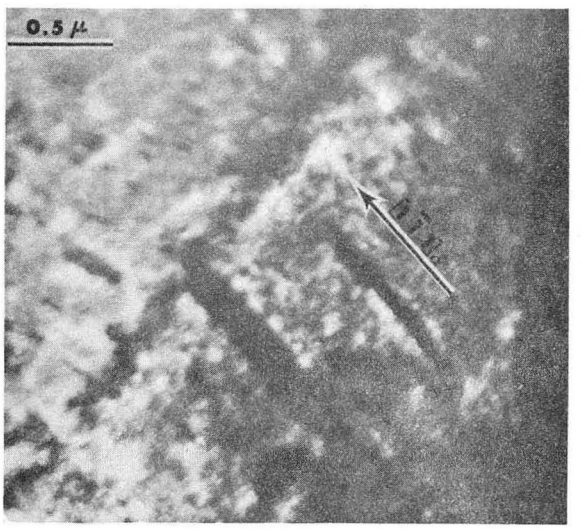

(a)

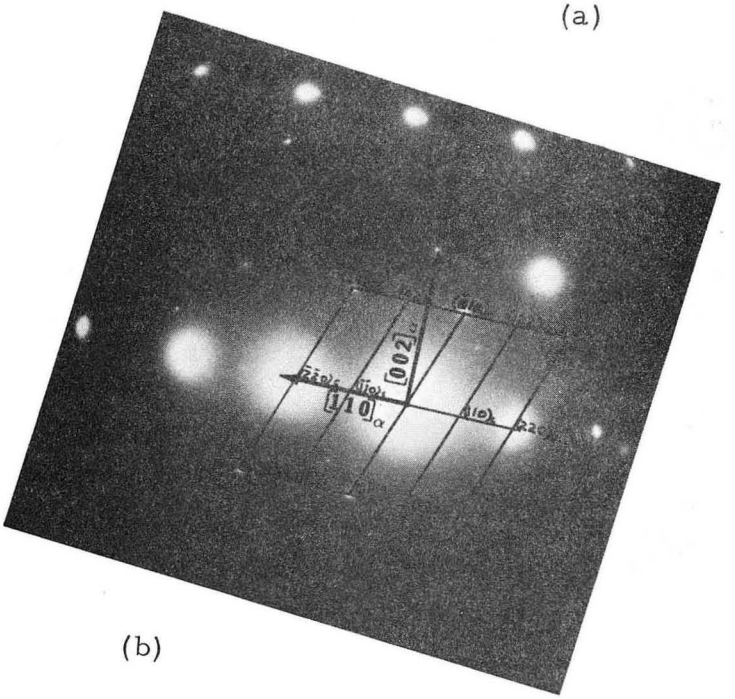

(b)

XBB 685-3015

Fig. 28 Thin foil micrographs of sample 13B; $\langle 110 \rangle_{orient}$

a) Bright field image showing large precipitates along $[1\bar{1}1]$ direction
b) Selected area diffraction with indexed cementite precipitate pattern

(a)

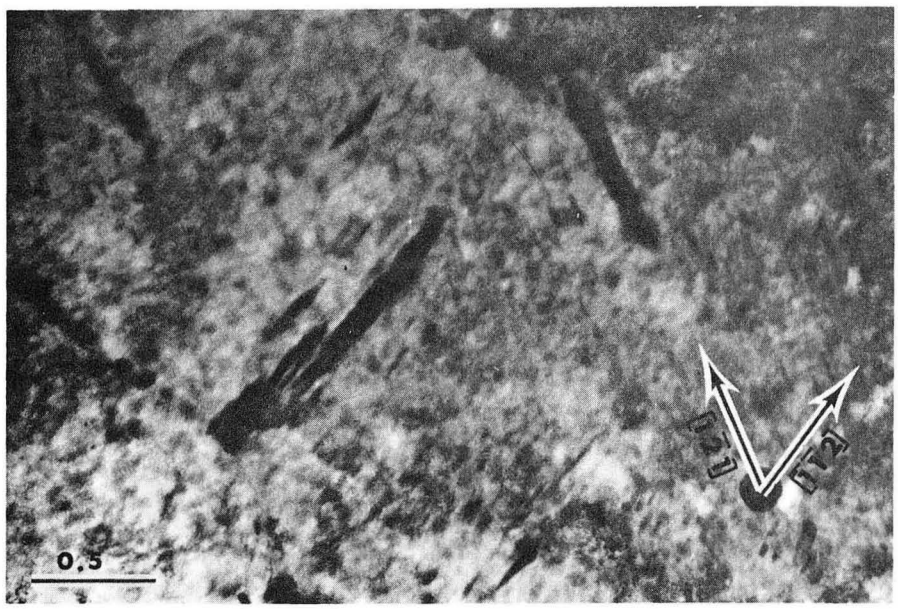

(b)

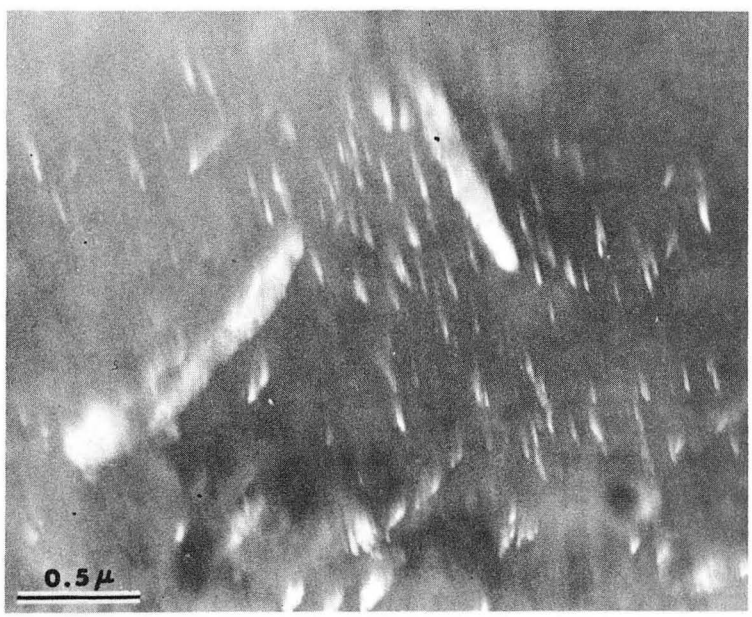

XBB 685-3021

Fig. 29 Thin foil micrographs of sample 12B; $\langle 111 \rangle_{orient}$

a) Bright field showing large precipitates along $\langle 211 \rangle$ directions

b) Dark field image of (a) showing precipitates

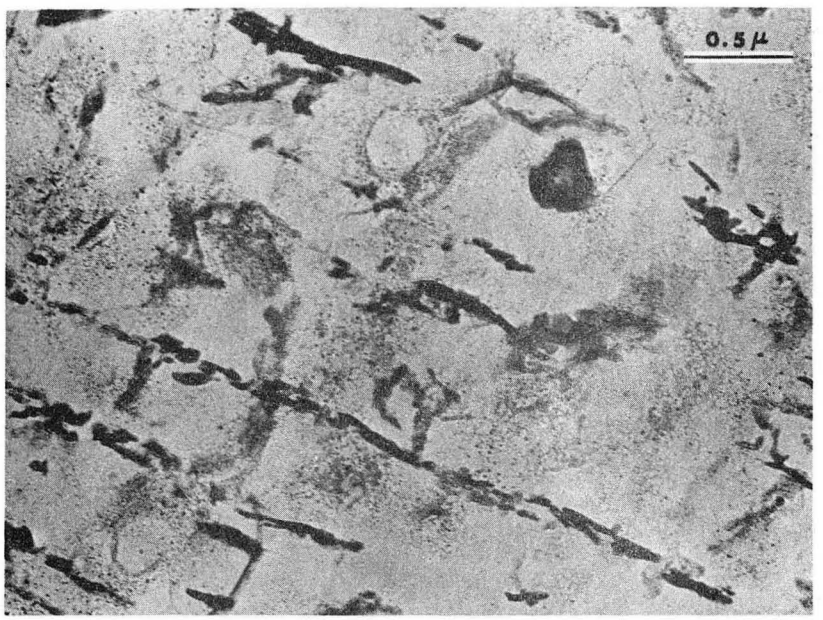

(a)

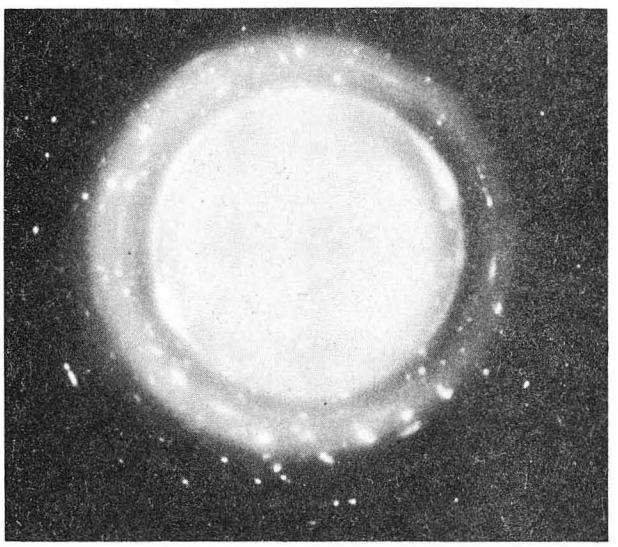

(b) XBB 685-3018

Fig. 30 Carbon extraction replica of sample 12B
a) Bright field image showing large grain boundary precipitates
b) Selected area diffraction of precipitate spots and gold rings

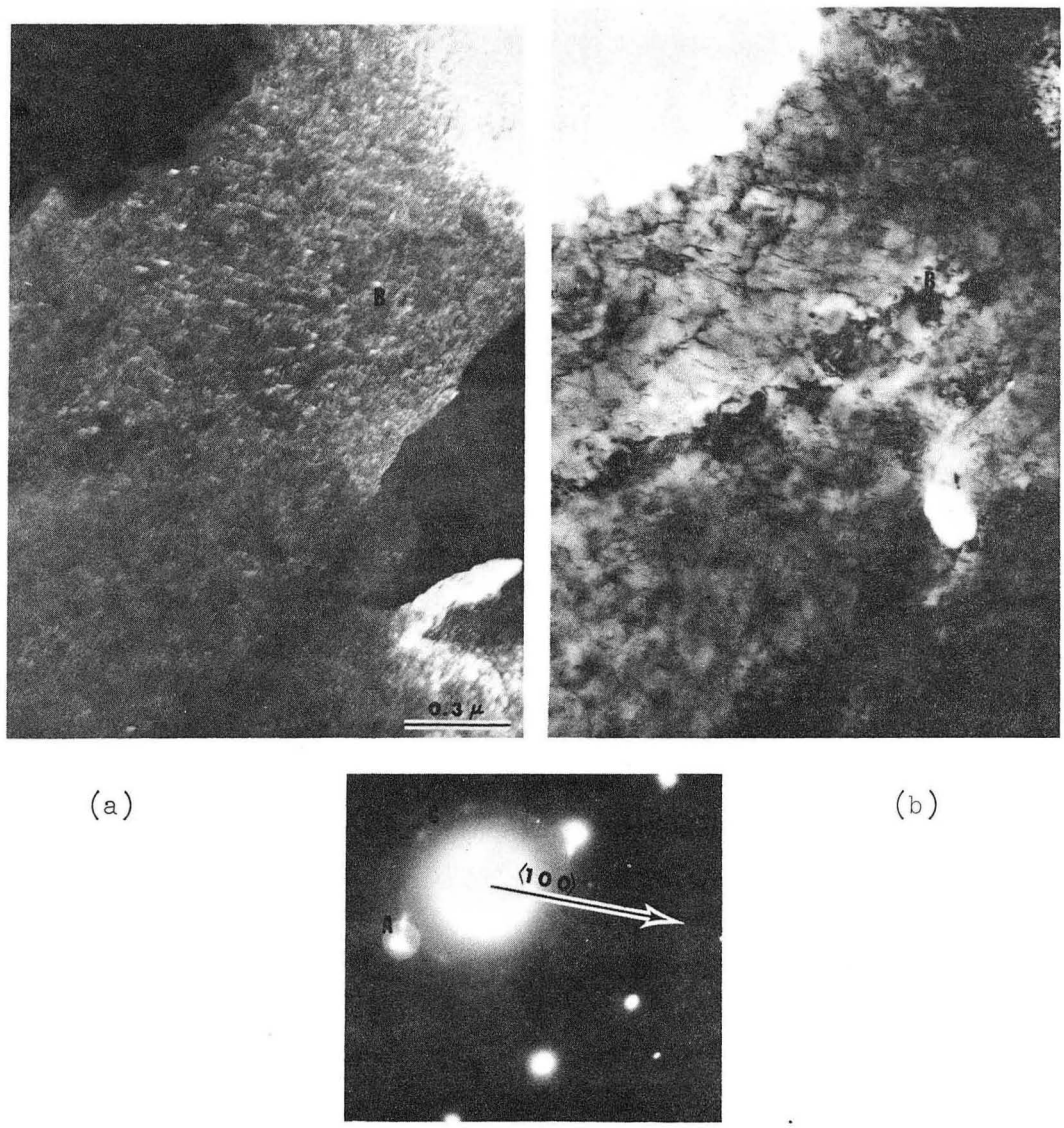

Fig. 31 Thin foil micrographs of sample 13B*; $\langle 311 \rangle_{orient}$

a) Dark field image of (b) dislocation precipitates, spherodized precipitates at "B"
b) Bright field image with dislocation precipitates, dissolution and spherodization of precipitates at "B"
c) Select area diffraction indicating ⟨100⟩ trace direction streaking of spots at "A", cementite spots at "C"

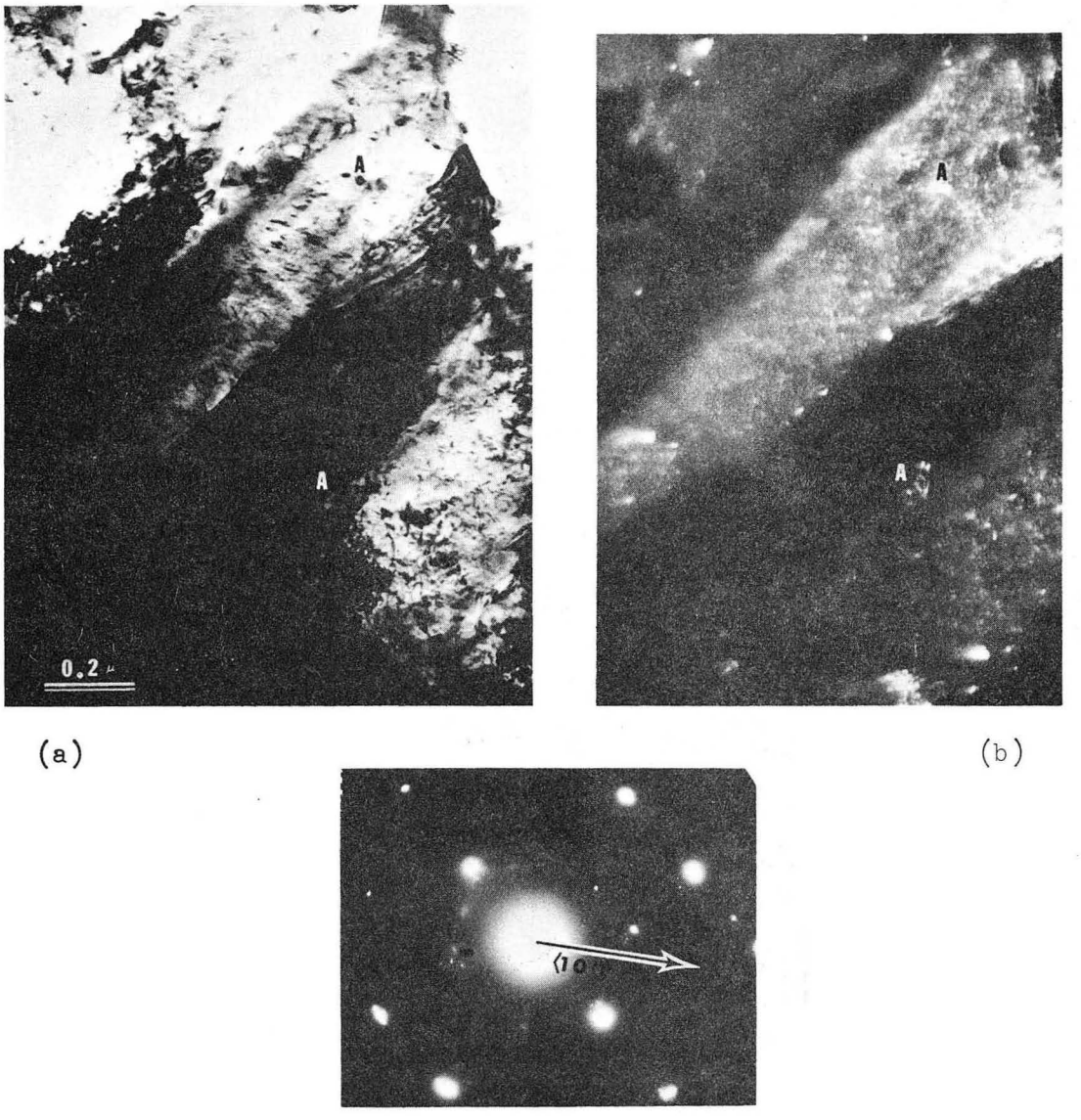

Fig. 32 Thin foil micrographs of sample 12B*; $\langle 311 \rangle_{orient}$

a) Bright field image showing precipitate, spherodized cementite precipitates at "A"
b) Dark field image of (a) due to spots at "B" in (c) showing precipitates at "A"
c) Selected area diffraction indicating ⟨100⟩ precipitate direction, streaking of precipitate spots at B